

# 1

## Introduction

Dark Matter is an enigma in modern physics. Despite the significant scientific effort that has gone into trying to discern its nature, a definitive detection proving its existence eludes us. Nevertheless, dark matter's influence on our Universe is undeniable, with evidence supporting its existence arising on **all** scales, large and small.

### 1.1 Evidence for Dark Matter

Today, the amount of evidence in support of dark matter's existence is overwhelming. This evidence comes from astrophysical and cosmological observations inconsistent with a universe composed entirely of visible matter. This section serves as a review of this evidence.

#### 1.1.1 Astrophysical Observations

##### Galaxy Clusters

Some of the first hints of dark matter's existence came from observations of galaxy clusters. Perhaps the most famous analysis was performed by Fritz Zwicky [1], who was puzzled by the high rotational velocities of galaxies within the Coma Cluster. By applying the virial theorem, equating the cluster's kinetic and gravitational potential energies, he found that the cluster would need to contain a much more significant amount of *dunkle materie* (dark matter) than visible matter to accommodate these high velocities.

## Rotation Curves of Spiral Galaxies

The anomalous rotational velocities observed in galaxy clusters can also be observed at the galactic scale. The rotation curves of spiral galaxies, which relate the rotational velocities of stars to their distance from the galactic centre, were observed to be flat at large distances. From the observed distribution of visible matter, Newtonian mechanics predicts that the orbital velocity of a star a distance  $r$  from the galactic centre,  $v_*(r)$ , is related to the mass of the galaxy,  $M(r)$ , through

$$v_*(r) = \sqrt{\frac{GM(r)}{r}}, \quad (1.1)$$

indicating that the velocity should fall off as  $1/\sqrt{r}$  at the outer regions of the galaxy where  $M(r)$  is constant. Instead, observations of many spiral galaxies indicate that this velocity remains constant out to the galaxy's edge.

A simple way to produce such a rotation curve is to introduce a spherically symmetric distribution of dark matter around the galaxy,

$$\rho_{\text{DM}}(r) = \frac{v_0^2}{4\pi Gr^2}, \quad (1.2)$$

that results in a constant rotational velocity of  $v_0$  out to the galaxy edge. Detailed simulations of structure formation in a Cold Dark Matter (CDM) Universe indicate that the dark matter halo follows a Navaro-Frenk-White (NFW) profile, [cite for NFW](#)

$$\rho_{\text{DM}}(r) = \frac{\rho_0}{\left(\frac{r}{r_s}\right)\left(1 + \frac{r}{r_s}\right)^2}, \quad (1.3)$$

where  $\rho_0$  and  $r_s$  are free parameters that must be fit to each halo.

An example rotation curve for galaxy NGC 6503 is presented in Fig. 1.1, with the contributions from each of the matter components to the rotational velocity shown [2, 3]. As can be seen, the visible matter constituting disk and gas components does not explain the observed rotational velocity.

## Gravitational Lensing

As General Relativity describes, the curvature of space-time around massive entities causes light to travel along curved paths. As such, the mass of astrophysical structures can be deduced from the extent to which objects in the background are gravitationally lensed. The disparity between the mass obtained from gravitational lensing and the mass of visible matter in the system is further evidence of dark matter's existence.

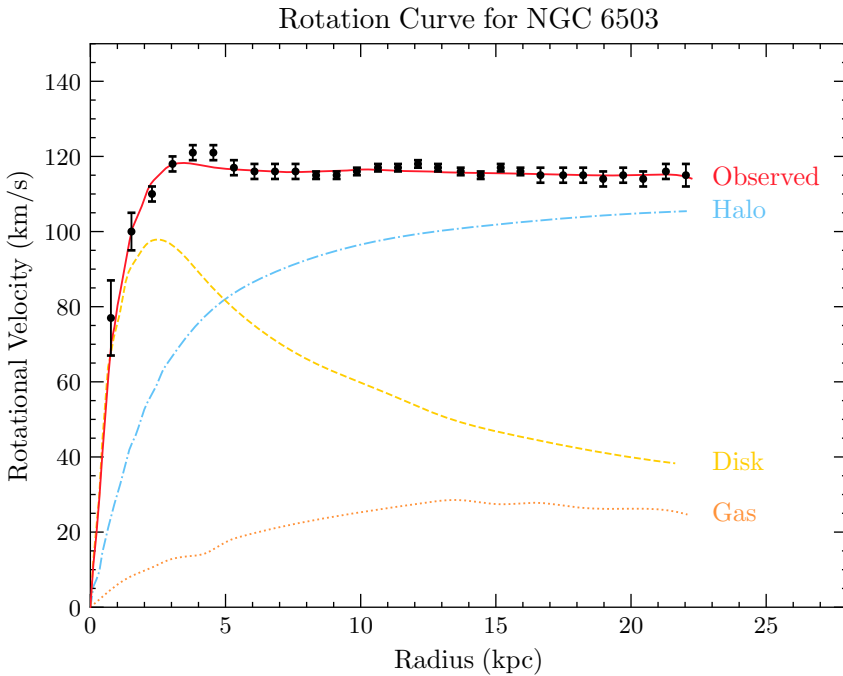


**Figure 1.1:** Galaxy rotation curve for NGC 6503, showing the contributions to the total velocity (red) from the DM halo (blue), disk (yellow), and gas components. Data used in making this plot was obtained from [2, 3].

### The Bullet Cluster

The bullet cluster is the result of two colliding galaxy clusters which the Chandra X-ray telescope imaged. When viewed in the X-ray, the smearing of the visible matter after the collision is clearly seen, as shown in the red regions of Fig. 1.2, which is expected from such a collision. However, when the gravitational potential was mapped using gravitational lensing, it was clear that the majority of the mass was displaced relative to the visible matter. This mass is attributed to the dark matter components of the original clusters. As indicated by the purple regions in Fig. 1.2, the dark matter halos seem to have passed through each other mostly unperturbed. This tells us that not only is the majority of the mass comprised of dark matter, but that the dark matter has extremely small interactions with both the visible matter and itself.

#### 1.1.2 Cosmological Evidence

Dark matter has played a major role in the cosmological history of our Universe. The current best cosmological model is the  $\Lambda$ -Cold Dark Matter model ( $\Lambda$ CDM), in

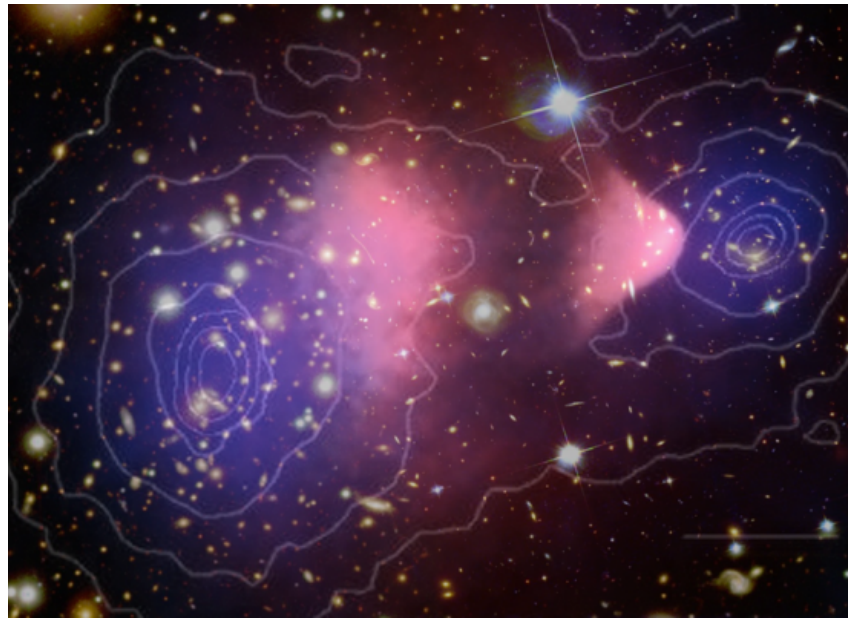


**Figure 1.2:** Image of the Bullet Cluster with contours of the gravitational potential superposed. The red regions indicate the baryonic matter after the collision, while the purple regions are the expected DM components deduced from gravitational lensing. [cite](#)

which cold (i.e. non-relativistic) dark matter plays a prominent role. The relative amount of dark matter present in our Universe can be determined with measurements of the light element abundances produced via Big Bang Nucleosynthesis (BBN).

### The Cosmic Microwave Background

One of the best probes of cosmological models is the Cosmic Microwave Background (CMB). The CMB is the radiation that was emitted during recombination when the Universe had cooled enough for electrons and protons to combine and not be ionised by the photon bath. While the CMB temperature looks isotropic on large scales, fluctuations around the average value of  $T_{\text{CMB}} \sim 2.73 \text{ K}$  are observed at very small scales. These anisotropies are the result of oscillations in the baryonic matter known as Baryon Acoustic Oscillations (BAO). These oscillations were produced due to the interplay between the outward pressure caused by matter interactions and the pull of gravitation due to dark matter.

Measuring the angular power spectra of these anisotropies and fitting the cosmological parameters of the  $\Lambda\text{CDM}$  model tell us how the Universe's energy density

$(\Omega_{\text{total}})$ , is partitioned between the matter ( $\Omega_m$ ), radiation ( $\Omega_{\text{rad}}$ ), and dark energy ( $\Omega_\Lambda$ ) components. In a flat universe, of which we believe ours to be, these components should sum to  $\Omega_{\text{tot}} = 1$ . The Planck collaboration most recently performed a precise measurement of the CMB power spectrum in 2018, obtaining best-fit parameters

$$\Omega_m = 0.311 \pm 0.006, \quad \Omega_\Lambda = 0.689 \pm 0.006. \quad (1.4)$$

Combining the predicted baryon density from BBN with the CMB observations breaks down the matter abundance into the dark ( $\Omega_{\text{DM}}$ ) and baryonic ( $\Omega_b$ ) components yielding

$$\Omega_{\text{DM}}h^2 = 0.1193 \pm 0.0009, \quad \Omega_{\text{DM}}h^2 = 0.02242 \pm 0.00014, \quad (1.5)$$

where  $h$  is the dimensionless Hubble constant such that the Hubble parameter today is  $H_0 = 100 h \text{ km s}^{-1} \text{ Mpc}$ .

## Large Scale Structure

After recombination, the pressure on the baryonic matter from photons subsided, allowing the small density perturbations to grow. This would lead to the growth of stars, galaxies, and the large-scale structure we observe today [4]. N-body simulations of the Universe's evolution require a cold dark matter component for this structure to form. While a small component of the dark matter can be warm, hot dark matter would wash out small-scale structures [5].

## 1.2 Potential Models of Dark Matter

The general consensus amongst physicists is that dark matter has a particle nature, similar to the visible matter of the Standard Model. Models may be as simple as dark matter being described by a single field or there could be an extensive hidden sector with complicated symmetry structures. Given the few details we know about dark matter, there exists an enormous library of models that can produce a viable dark matter candidate. However, there are generic properties a good dark matter candidate must satisfy, namely:

- **Stable on Cosmological Timescales:** Dark matter must either be stable or have a lifetime significantly longer than the age of the Universe in order to be present in its current abundance.

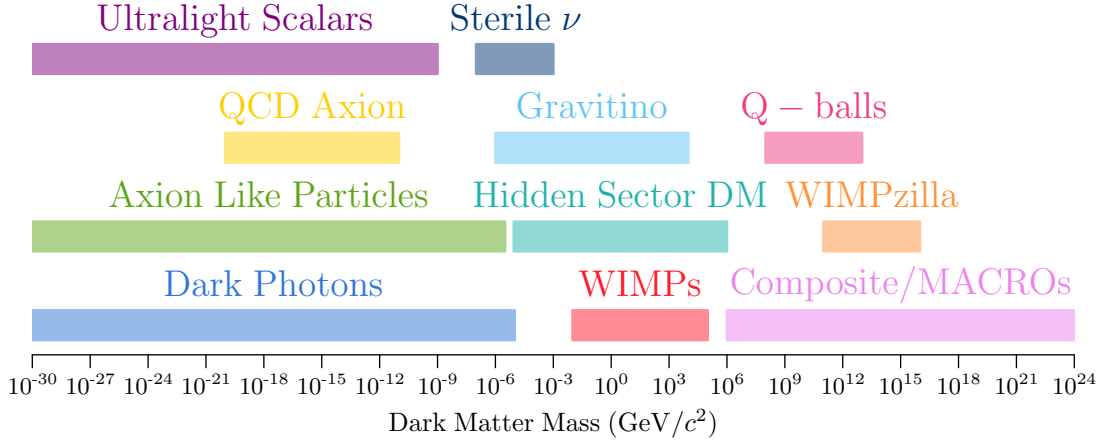


**Figure 1.3:** Illustrative landscape of dark matter models and the mass range for which they predict a valid candidate.

- **Neutral or milli-charged under Electromagnetism:** Dark matter, as its name suggests, does not significantly interact with light. By requiring that dark matter be completely decoupled from the Standard Model plasma by the time of recombination yields an upper bound on the milli-charge dark matter can carry of [6]

$$q_{\text{DM}}/e < \begin{cases} 3.5 \times 10^{-7} \left(\frac{m_{\text{DM}}}{1 \text{ GeV}}\right)^{0.58}, & m_{\text{DM}} > 1 \text{ GeV} \\ 4.0 \times 10^{-7} \left(\frac{m_{\text{DM}}}{1 \text{ GeV}}\right)^{0.35}, & m_{\text{DM}} < 1 \text{ GeV}, \end{cases} \quad (1.6)$$

- **Small Self-Interactions:** The standard  $\Lambda\text{CDM}$  cosmology assumes that the dark matter is collisionless. However, small dark matter self-interactions can help resolve existing small-scale structure issues [7, 8]. Current limits on the self-interaction cross section are  $\sigma_{\text{DM-DM}}/m_{\text{DM}} < 0.48 \text{ cm}^2/\text{g}$  come from merging galaxy clusters [9] and the ellipticity of galaxies obtained from X-ray observations [10].

A selection of the more prominent dark matter candidates is shown in Fig. 1.3. The key features of a few of these models are discussed below.

## WIMPs

The Weakly Interacting Massive Particle (WIMP) is perhaps the most well-known dark matter candidate. WIMPs rose to fame thanks to the so-called “WIMP miracle” [11]. This refers to the fact that particles with weak scale masses and annihilation cross sections just so happen to have the correct relic abundance of dark

matter when produced via the freeze-out mechanism [12]. In this scenario, the final WIMP abundance depends on the total annihilation cross-section,  $\langle\sigma v\rangle$ , with only a very mild dependence on the DM mass [13],

$$\Omega_{\text{DM}} h^2 \sim 0.12 \left( \frac{2.2 \times 10^{-26} \text{ cm}^3 \text{ s}^{-1}}{\langle\sigma v\rangle} \right). \quad (1.7)$$

The canonical weak-scale WIMP has been tightly constrained from direct and indirect detection limits, leading it to be disfavoured as a dark matter candidate. The term “WIMP” is now typically used to refer to any particle dark matter candidate that is produced thermally in the early Universe. Such a particle can have a mass in the range  $10 \text{ MeV} \lesssim m_{\text{WIMP}} \gtrsim 100 \text{ TeV}$ . Lighter WIMPs will have non-negligible contributions to the effective number of neutrino species,  $N_{\text{eff}}$ , which is constrained through BBN and the Cosmic Microwave Background CMB to be  $N_{\text{eff}} = 2.99 \pm 0.17$  [14]. Masses larger than  $\sim 100 \text{ TeV}$  are excluded from partial wave unitarity [15].

## Axions

The original axion was proposed by Peccei and Quinn [16] as part of a dynamical solution to the “Strong CP Problem”. This refers to the measured value of the neutron electric dipole moment (nEDM) being anomalously small, with a current upper bound of  $|d_n| < 0.18 \times 10^{-26} e \text{ cm}$  [17]. This can be translated to an upper bound on the CP-violating QCD  $\theta$ -parameter such that  $|\theta_{\text{QCD}}| \lesssim 10^{-10}$ , raising questions as to why this value seems to be fine-tuned to such a small value.

The Peccei-Quinn solution to this problem introduces a new, anomalous, global  $U(1)_{\text{PQ}}$  symmetry and promotes  $\theta_{\text{QCD}}$  to be a dynamical field. The axion emerges as the pseudo-Goldstone boson associated with the breaking of  $U(1)_{\text{PQ}}$ , such is in the two most prominent UV completions of the axion, the KSVZ [18, 19] and DFSZ [20, 21] models. In these models, the axion produced in the early Universe can serve the role of cold dark matter today. This makes it a very compelling dark matter candidate, as it solves two of the biggest mysteries of physics in one neat package.

However, solving the Strong CP problem can be rather restrictive on the model parameters. For example, the QCD axion’s coupling to the photon is not a free parameter and depends on the scale at which the PQ symmetry is broken. Many models introduce a light pseudoscalar particle that is not associated with a solution to the Strong CP problem but has a coupling to the photon that takes the same form as the QCD axion. Such pseudoscalars are known as “Axion Like Particles” (ALPs) and can similarly make a good dark matter candidate.

**Add some more candidates**

### 1.2.1 Dark Matter in an Effective Fields Theory Framework

### 1.2.2 Overview of Effective Field Theory

Given the sheer quantity of potential dark matter models and candidates, a model-independent approach for analysing experimental results is often desired. An economic analysis method is to use an Effective Field Theory (EFT) to describe the dark matter-Standard Model interactions. Effective theories are prevalent in all of physics, e.g., describing light using ray optics vs Maxwell's equations or the orbits of planets using Newtonian gravity vs General relativity. The delineating factor in choosing a formalism is the scale (energy, length, etc.) we are interested in. **Add in the usual EFT diagram** Experiments will only be sensitive to interactions that can occur below some energy scale, i.e. 13.6 TeV at the LHC or 1 GeV in direct detection experiments; we are only interested in describing the interactions that occur below this scale.

One follows two main schools of thought when constructing an EFT. First, there is the *top-down* approach. Here, you begin with a particular complete model in mind that consists of heavy and light fields. At energies below the production threshold of the heavy fields, these degrees of freedom can be “integrated out” of the theory. This process leaves an effective theory for the interactions amongst the light fields. The interactions that would be mediated by the heavy fields appear as non-renormalisable operators that are suppressed by this high energy scale,  $\Lambda$ .

The second method, known as the *bottom-up* approach, is more agnostic to the high-energy physics that might be in play. In this method, one constructs all possible operators that obey the required symmetries of the theory up to a desired mass dimension. Operators of mass dimension greater than four are then suppressed by powers the required number of powers of the high energy cutoff scale,  $\Lambda$ . This cutoff scale indicates the energy at which the EFT begins to break down and should at least be larger than the masses of the fields in the EFT. The Lagrangian constructed in this manner is made out of a tower of operators,  $\mathcal{O}_i^{(n)}$ , forming

$$\mathcal{L}_{\text{EFT}} \supset \sum_{n>4} \sum_{i=1}^{j_n} \frac{C_i^{(n)}}{\Lambda^{n-4}} \mathcal{O}_i^{(n)}, \quad (1.8)$$

where we sum over all  $j_n$  operators present at mass dimension  $n$ . The  $C_i^{(n)}$  are called Wilson coefficients and are typically energy dependent.

In the context of dark matter, there are many EFTs describing the interaction at various energy scales. For example, dark matter scattering off nuclei in direct detection experiments is described by a non-relativistic EFT built out of the momentum transfer, relative velocity and spin operators of the dark matter and targets [22,

[23]. At higher energy scales where relativistic effects become important, the EFT is instead constructed from relativistic fields, such as dark matter that may be produced in colliders.

Generally, an EFT will have fewer free parameters than the underlying UV theories, typically the dark matter mass and the high energy cutoff scale. This is in contrast with the dozens or so parameters often present in complete models. This allows for a simpler interpretation of experimental results as you will be fitting to a lower dimensional parameter space.

[Move the next sections later?](#)

### 1.2.3 Dimension 6 EFT Operators for Dirac Fermion Dark Matter

This work's approach will focus on dimension 6 EFT operators that describe the interactions of Dirac fermion dark matter with standard model fermions. These operators will have a structure

$$\mathcal{L}_{\text{EFT}}^{(6)} \sim \frac{1}{\Lambda^2} (\bar{\chi} \Gamma_{\text{DM}} \chi) (\bar{f} \Gamma_{\text{SM}} f), \quad (1.9)$$

where the  $\Gamma_i$  determines the Lorentz structure of the interaction by taking appropriate combinations from the set

$$\Gamma_i \in \{1, i\gamma_5, \gamma^\mu, i\gamma^\mu\gamma^5, \sigma^{\mu\nu}, i\sigma^{\mu\nu}\gamma^5\}. \quad (1.10)$$

For example, the case of  $\Gamma_\chi = \Gamma_{\text{SM}} = 1$  yields scalar currents for both the DM and SM fermions and would correspond to integrating out a heavy scalar mediator in the UV theory. There are 10 such operators at dimension six that form a linearly independent basis. These are given in Table 1.1, along with spin-averaged squared matrix element for dark matter scattering with a fermion. The coupling constants,  $g_f$ , are given in terms of the fermion Yukawa couplings,  $y_f$ , and the EFT cutoff scale,  $\Lambda_f$ . Hence, these operators describe interactions between dark matter and the elementary fermions of the Standard Model: the leptons and quarks.

### 1.2.4 Going from DM-Quark to DM-Nucleon Interactions

The operators in Table 1.1 describe dark matter interactions at the quark level, as these are the degrees of freedom most models are formulated with. However, we will primarily be interested in dark matter scattering with baryons, which requires taking the matrix element of the quark operators between baryon states,

Name	Operator	$g_f$	$ \overline{M}(s, t, m_i) ^2$
D1	$\bar{\chi}\chi \bar{f}f$	$\frac{y_f}{\Lambda_f^2}$	$g_f^2 \frac{(4m_\chi^2 - t)(4m_\chi^2 - \mu^2 t)}{\mu^2}$
D2	$\bar{\chi}\gamma^5\chi \bar{f}f$	$i \frac{y_f}{\Lambda_f^2}$	$g_f^2 \frac{t(\mu^2 t - 4m_\chi^2)}{\mu^2}$
D3	$\bar{\chi}\chi \bar{f}\gamma^5 f$	$i \frac{y_f}{\Lambda_f^2}$	$g_f^2 t (t - 4m_\chi^2)$
D4	$\bar{\chi}\gamma^5\chi \bar{f}\gamma^5 f$	$\frac{y_f}{\Lambda_f^2}$	$g_f^2 t^2$
D5	$\bar{\chi}\gamma_\mu\chi \bar{f}\gamma^\mu f$	$\frac{1}{\Lambda_f^2}$	$2g_f^2 \frac{2(\mu^2 + 1)^2 m_\chi^4 - 4(\mu^2 + 1)\mu^2 s m_\chi^2 + \mu^4(2s^2 + 2st + t^2)}{\mu^4}$
D6	$\bar{\chi}\gamma_\mu\gamma^5\chi \bar{f}\gamma^\mu f$	$\frac{1}{\Lambda_f^2}$	$2g_f^2 \frac{2(\mu^2 - 1)^2 m_\chi^4 - 4\mu^2 m_\chi^2 (\mu^2 s + s + \mu^2 t) + \mu^4(2s^2 + 2st + t^2)}{\mu^4}$
D7	$\bar{\chi}\gamma_\mu\chi \bar{f}\gamma^\mu\gamma^5 f$	$\frac{1}{\Lambda_f^2}$	$2g_f^2 \frac{2(\mu^2 - 1)^2 m_\chi^4 - 4\mu^2 m_\chi^2 (\mu^2 s + s + t) + \mu^4(2s^2 + 2st + t^2)}{\mu^4}$
D8	$\bar{\chi}\gamma_\mu\gamma^5\chi \bar{f}\gamma^\mu\gamma^5 f$	$\frac{1}{\Lambda_f^2}$	$2g_f^2 \frac{2(\mu^4 + 10\mu^2 + 1)m_\chi^4 - 4(\mu^2 + 1)\mu^2 m_\chi^2 (s + t) + \mu^4(2s^2 + 2st + t^2)}{\mu^4}$
D9	$\bar{\chi}\sigma_{\mu\nu}\chi \bar{f}\sigma^{\mu\nu} f$	$\frac{1}{\Lambda_f^2}$	$8g_f^2 \frac{4(\mu^4 + 4\mu^2 + 1)m_\chi^4 - 2(\mu^2 + 1)\mu^2 m_\chi^2 (4s + t) + \mu^4(2s + t)^2}{\mu^4}$
D10	$\bar{\chi}\sigma_{\mu\nu}\gamma^5\chi \bar{f}\sigma^{\mu\nu} f$	$\frac{i}{\Lambda_f^2}$	$8g_f^2 \frac{4(\mu^2 - 1)^2 m_\chi^4 - 2(\mu^2 + 1)\mu^2 m_\chi^2 (4s + t) + \mu^4(2s + t)^2}{\mu^4}$

**Table 1.1:** Dimension 6 EFT operators [24] for the coupling of Dirac DM to fermions (column 2), together with the squared matrix elements DM-fermion scattering (column 5), where  $s$  and  $t$  are Mandelstam variables,  $\mu = m_\chi/m_T$ , and  $m_T$  is the target mass.

i.e.  $\langle \mathcal{B} | \bar{q} \Gamma_q q | \mathcal{B} \rangle$ . These matrix elements can be calculated through the application of Chiral Perturbation Theory (ChPT), giving a baryon level EFT. The operators of this EFT will have the same form as those in Table 1.1, with the obvious replacement of  $f \rightarrow \mathcal{B}$ , as well as additional form factors that take into account the structure of the baryons.

The required form factors for each operator have been calculated at zero mo-

momentum transfer in Ref. [22] and are given by

$$c_{\mathcal{B}}^S(0) = \frac{2m_{\mathcal{B}}^2}{v^2} \left[ \sum_{q=u,d,s} f_{T_q}^{(\mathcal{B})} + \frac{2}{9} f_{T_G}^{(\mathcal{B})} \right]^2, \quad (1.11)$$

$$c_{\mathcal{B}}^P(0) = \frac{2m_{\mathcal{B}}^2}{v^2} \left[ \sum_{q=u,d,s} \left( 1 - 3 \frac{\bar{m}}{m_q} \right) \Delta_q^{(\mathcal{B})} \right]^2, \quad (1.12)$$

$$c_{\mathcal{B}}^V(0) = 9, \quad (1.13)$$

$$c_{\mathcal{B}}^A(0) = \left[ \sum_{q=u,d,s} \Delta_q^{(\mathcal{B})} \right]^2, \quad (1.14)$$

$$c_{\mathcal{B}}^T(0) = \left[ \sum_{q=u,d,s} \delta_q^{(\mathcal{B})} \right]^2, \quad (1.15)$$

where  $v = 246$  GeV is the vacuum expectation value of the SM Higgs field,  $\mathcal{B}$  is the baryonic species,  $\bar{m} \equiv (1/m_u + 1/m_d + 1/m_s)^{-1}$  and  $f_{T_q}^{(\mathcal{B})}$ ,  $f_{T_G}^{(\mathcal{B})} = 1 - \sum_{q=u,d,s} f_{T_q}^{(\mathcal{B})}$ ,  $\Delta_q^{(\mathcal{B})}$  and  $\delta_q^{(\mathcal{B})}$  are the hadronic matrix elements, determined either experimentally or by lattice QCD simulations<sup>1</sup>. The specific values of these matrix elements for various baryons are provided in Appendix **ADD APPENDIX**.

These form factors are perfectly viable when considering interactions with momentum transfers  $\lesssim 1$  GeV such as in direct detection experiments. For energies greater than this, the internal structure of the baryon begins to be resolved, and an additional momentum-dependent form factor is required to account for this [25],

$$F_{\mathcal{B}}(t) = \frac{1}{(1 - t/Q_0)^2}, \quad (1.16)$$

where  $t$  is the Mandelstam variable, and  $Q_0$  is an energy scale that depends on the hadronic form factor. For simplicity, we will conservatively take  $Q_0 = 1$  GeV for all operators. Putting everything together, the squared coupling constants for dark matter-baryon interactions are obtained by making the replacement

$$g_f^2 \rightarrow \frac{c_{\mathcal{B}}^I(t)}{\Lambda_q^4} \equiv \frac{1}{\Lambda_q^4} c_{\mathcal{B}}^I(0) F_{\mathcal{B}}^2(t), \quad I \in S, P, V, A, T, \quad (1.17)$$

in the matrix elements in the final column of Table 1.1.

---

<sup>1</sup>The superscript letters  $S$ ,  $P$ ,  $V$ ,  $A$  and  $T$  stand for Scalar, Pseudoscalar, Vector, Axial-vector and Tensor interactions respectively. The corresponding operators are: D1-2 for  $S$ ; D3-4 for  $P$ ; D5-6 for  $V$ , D7-8 for  $A$ ; and D9-10 for  $T$ .

## 1.3 Current Status of Dark Matter Constraints

In broad terms, there are three main ways that we can search for evidence of dark matter, often termed “make it, shake it or break it”. “Make it” refers to dark matter being produced at colliders; “break it” to searching for dark matter annihilation signals; and “shake it” to direct detection of dark matter scattering. An illustrative way of depicting these processes is shown in Fig. [add usual diagram](#). This section discusses the current status of these detection methods.

### 1.3.1 Collider Bounds

If dark matter is produced in a collider, it will simply leave the detector without depositing any energy. In order to determine if such an invisible particle was produced, conservation of energy-momentum is used to determine if there are any events that are missing energy. In practice, what is searched for is missing momentum that is transverse to the beamline.

Currently, dark matter has not been observed to be produced in particle colliders. This non-observation has instead been used to constrain the dark matter mass and production cross sections or couplings of various models. These limits are typically interpreted in a model-dependent manner, as different dark matter - Standard model couplings can significantly alter the production rates. As mentioned above, EFTs can be used to explore a variety of interactions in a somewhat model-independent way. However, many applications of this nature did not hold up to scrutiny, as the EFTs were being applied at energies outside their regions of validity [26–29], and so care is needed when applying such methods.

The ATLAS and CMS experiments at the LHC have performed analyses on various dark matter production mechanisms, including the exchange of a  $Z/Z'$  or Higgs, EFTs and heavy mediators, and mono-jet searches [30]<sup>2</sup>. Collider searches also offer complimentary probes of the dark matter-nucleon scattering cross-section [31].

It is important to note that an observation of an invisible massive particle at a collider is not enough to infer that it is dark matter. Such an observation only tells us that such a particle exists but nothing about its abundance, meaning it could just be a sub-component of a larger dark sector. In order to identify whether or not this was a dark matter detection, complimentary observations from direct or indirect detectors would be required.

---

<sup>2</sup>These searches refer to a single jet being produced alongside a pair of dark matter particles. This jet could be of Standard Model or dark sector origin, with the latter commonly referred to as “mono-X” searches.

### 1.3.2 Direct Detection Searches

Direct detection experiments vary wildly depending on the dark matter mass range they are trying to probe. For ALP dark matter that is wavelike, haloscope experiments such as ADMX [32] and MADMAX [33] attempt to convert ALPs to photons via the Primakoff effect. Searches for WIMP dark matter look for the dark matter scattering with some detector material, causing it to recoil and release some energy. Given our focus on WIMP dark matter, this section will review the experimental status of these detectors.

The differential rate at which the incoming flux of dark matter will scatter within a detector with  $N_T$  targets, as a function of the recoil energy,  $E_R$ , is given by

$$\frac{dR(E_R, t)}{dE_R} = N_T \frac{\rho_{\text{DM}}}{m_{\text{DM}}} \int_{v > v_{\min}}^{v_{\text{esc}}} v f(\vec{v} + \vec{v}_E) \frac{d\sigma}{dE_R} d^3v, \quad (1.18)$$

and depends on the quantities:

- $v_{\min}$  is the minimum dark matter velocity required by kinematics for a scattering event to occur;
- $v_{\text{esc}} = 528 \text{ km s}^{-1}$  is the Milky Way escape velocity;
- $\vec{v}_E$  is the velocity of the Earth through the dark matter halo<sup>3</sup>;
- $f(\vec{v} - \vec{v}_E)$  is the dark matter velocity distribution in the Earth's frame;
- $d\sigma/dE_R$  is the differential scattering cross-section.

Given the low interaction rate of dark matter, the expected event rate in detectors is very low, around one event per day, per kilogram of target material, per kiloelectronvolt deposited. Having such a low event rate requires the detector to be situated in an extremely low background environment, such as underground laboratories.

Direct detection experiments aim to probe two main types of dark matter interactions: Spin-dependent (SD) and spin-independent (SI) scattering. SD interactions couple to the overall spin of the target, while SI interactions are agnostic to this. Therefore, experiments searching for SI interactions benefit from using nuclei with a large atomic number,  $A$ , as the interaction cross-section will involve a coherent sum over all nucleons. This leads to an  $A^2$  enhancement of SI interactions compared to the SD counterpart.

---

<sup>3</sup>This accounts for the orbit of the Earth around the Sun, which induces an annual modulation in the flux of DM.

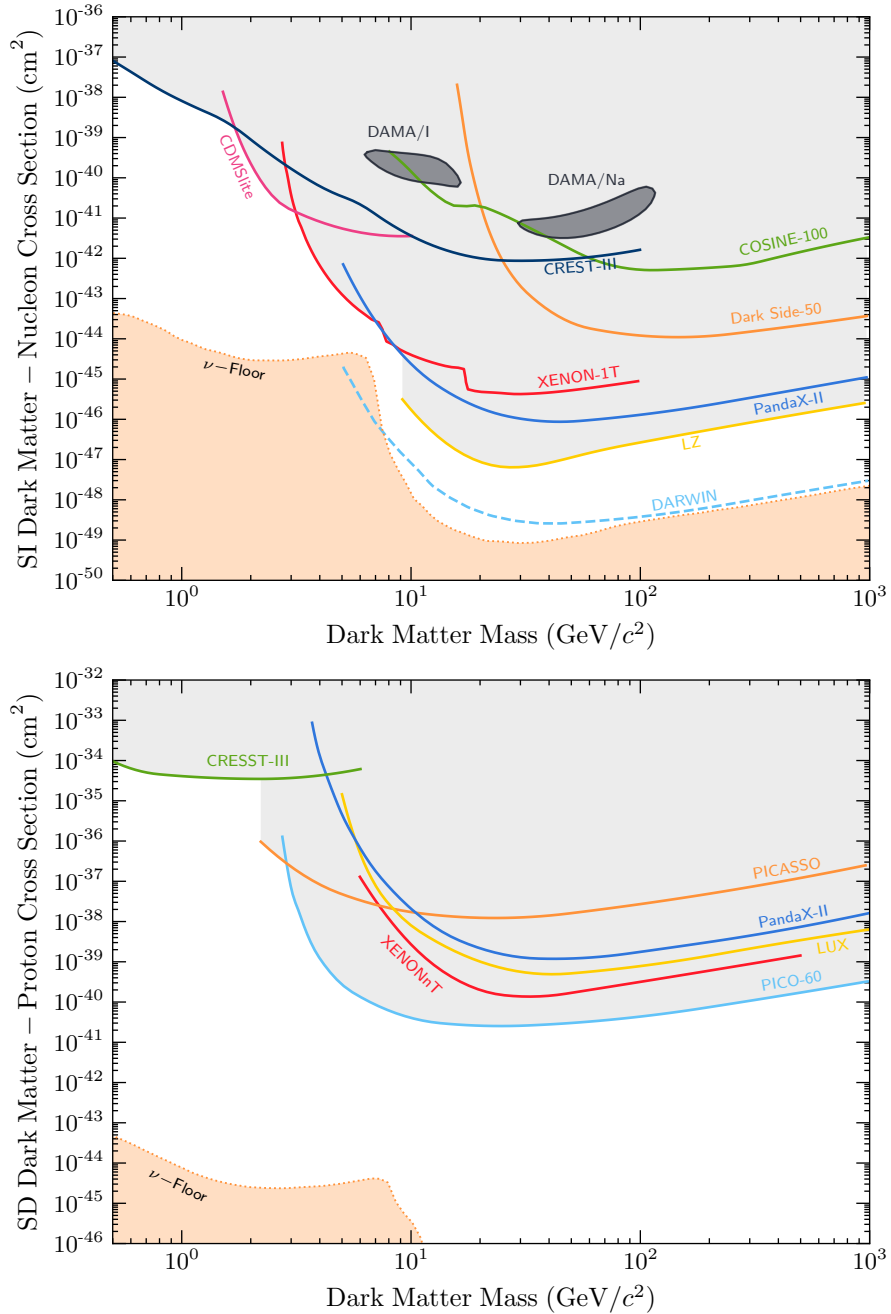


**Figure 1.4:** Current status of direct detection searches for dark matter. **Top:** Spin-independent dark matter-nucleon scattering. **Bottom:** Spin-dependent dark matter-proton scattering.

The current leading constraints on the dark matter-nucleon scattering cross-section are shown in Fig. 1.4, with SI in the top panel and SD in the bottom. The SI limits are set by liquid noble gas experiments (LZ [34], XENON-1T [35], PandaX-II [36], and DarkSide-50 [37]), solid-state cryogenic detectors (CRESST-III [38], CDMSlite [39], with projected DARWIN sensitivities [40]), and room temperature crystals (DAMA/LIBRA [41], and COSINE-100 [42]).

The SD experiments require their targets to carry non-zero spin for the dark matter to couple to.  $^{19}\text{F}$  is the favourable choice proton scattering, as it has an unpaired proton giving it its overall spin. The leading constraints come from superheated liquid experiments such as the PICO-60 [43] as well as PICASSO [44]. In terms of the SD proton scattering shown in Fig 1.4, These interactions are also searched for by many of the same experiments in the SI case, with the inclusion of LZ’s predecessor LUX [45].

The orange dashed line represents the neutrino floor<sup>4</sup>, a theoretical lower limit on the discoverability of WIMP-like dark matter. In this region of parameter space, doctors will become sensitive to the irreducible background from neutrino scattering, which will produce signals almost indistinguishable from a true dark matter interaction. A significant amount of effort is being put toward overcoming this hindrance, with the main strategy being to take advantage of the directionality of dark matter flux [47].

Many experiments begin to lose sensitivity to low-mass dark matter ( $m_{\text{DM}} \lesssim 10 \text{ GeV}$ ) as the targets recoil with energies below the detector threshold. Current energy thresholds can reach as low as  $\sim \mathcal{O}(100 \text{ eV})$ , which is on the same order of magnitude as the recoil energy due to a 1 GeV dark matter collision. The sensitivity also falls off at a slower rate at larger masses, though this is due to the number of dark matter particles that pass through the detector given  $N_{\text{DM}} = \rho_{\text{DM}}/m_{\text{DM}}$ , and the dark matter density is known to be  $0.4 \text{ GeV cm}^{-3}$ .

Direct detection limits also assume that the scattering cross-section is independent of the dark matter velocity and momentum transfer in the interaction. Given that the local dark matter dispersion velocity is predicted to be  $v_d = 270 \text{ km s}^{-1} \approx 10^{-3}c$ , a back-of-the-envelope estimation for the momentum transfer gives  $q_{\text{tr}} \lesssim 100 \text{ MeV}$ . Therefore, cross-sections proportional to  $v_{\text{DM}}$  or  $q_{\text{tr}}$  will result in significantly lower event rates and hence much weaker limits than the unsuppressed interactions.

This leads us to indirect detection methods, which can provide complementary probes to direct detection while also exploring interactions that are difficult, if not impossible, for terrestrial-based detectors to observe.

---

<sup>4</sup>Calling this the “neutrino fog” rather than floor has been gaining traction in recent years [46]

### 1.3.3 Indirect Detection

Indirect detection experiments aim to infer the presence of dark matter through its annihilation or decay into Standard Model states. These searches look for anomalies in astrophysical data, though dark matter accumulating within the Earth's core can also produce a detectable signal [48, 49]. The signals searched for include:

- Gamma-rays at terrestrial-based telescopes such as HESS [50–52], VERITAS [53–55], MAGIC [56, 57] and HAWC [58–61] as well as the Fermi-LAT [62–66] satellite;
- Neutrino signals at IceCube [67, 68], ANTARES [49, 69, 70], Super-K [71–73], and will be searched for at the upcoming Hyper-K [74–76], JUNO [77] experiments.
- Cosmic-Rays by the AMS-02 experiment [78, 79]

Signals from dark matter annihilation are best searched for by looking at regions where the dark matter density is expected to be high, boosting the annihilation rate. Natural places to look include the Galactic Centre [80, 81], dwarf-spheroidal galaxies [82], and celestial bodies where dark matter can accumulate over time. This last option is of primary interest to this work.

Stars have long been used to study various models of dark matter. ALPs of dark photons can be produced within the plasma of stars, altering the energy transport properties within them. This can ultimately lead to deviations in the evolution of the star, which can be used to place some of the strongest constraints on these models [83–85]. WIMP-like dark matter from the halo that couples to visible matter can scatter within the objects. The dark matter may lose enough energy in these interactions to become gravitationally bound to the object, leading to a population of dark matter being accumulated over time [12, 86–89].

The capture of dark matter within the Sun has been extensively studied. The formalism set up by Gould [87, 88, 90] has remained quite successful, with many authors building on these foundations over time [89, 91, 92]. The captured dark matter can thermalise within the Sun's core, where it may annihilate and produce an observational signal. This could be via direct annihilation to neutrinos [69–71, 93, 94], or to some other long-lived state that can escape the Sun and decay into visible states [95–99]. Additionally, WIMPs can also alter the energy transport within the Sun [100–103].

In comparison to DD searches, interpretation of indirect detection data will require additional model-dependent assumptions, namely the relevant annihilation channels of the dark matter. The most general limits can be placed by assuming that the dark matter only has a single annihilation channel, i.e. it annihilates to a  $\tau^+\tau^-$  final state 100% of the time. Under these assumptions, limits on the SD dark

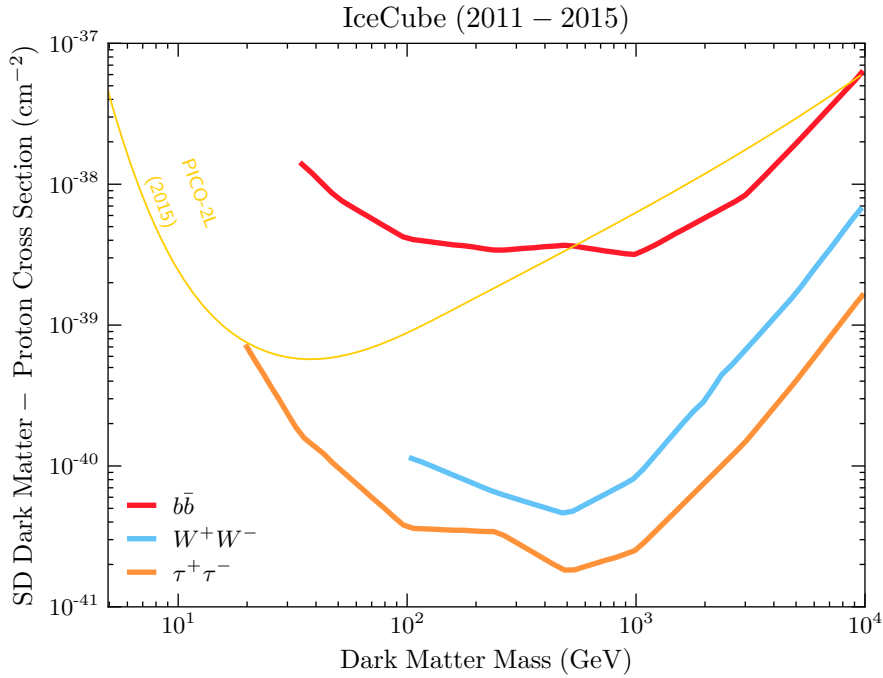


**Figure 1.5:** Limits on the SD dark matter-proton cross-section from the IceCube collaboration assuming 100% branching fraction to  $b\bar{b}$  (red),  $W^+W^-$  (blue) or  $\tau^+\tau^-$  (orange) final states. Also shown is the result from the PICO-2L DD experiment. This plot was recreated with data taken from Ref. [67].

matter-proton cross-section have been placed that exceed current DD constraints, due to the rather large abundance of Hydrogen within the Sun. Constraints from the IceCube collaboration are shown in Fig. 1.5

The smallest dark matter mass that can be probed using solar capture is determined by the evaporation mass of the Sun. Below this mass, the dark matter will be efficiently evaporated out of the Sun at the same rate it is captured, thus no annihilation can take place<sup>5</sup>. Additionally, as with direct detection, the Sun will be far less sensitive to interactions that are proportional to the velocity/momentum transfer.

Overcoming the first issue requires either a colder star or one that is much heavier. The second requires dark matter to scatter with the constituent material at relativistic energies to overcome the suppression in the cross-sections. Fortunately, there exists objects that meet all these criteria, allowing for a wider variety of dark matter models to be explored than direct detection or traditional indirect detection experiments: compact objects.

<sup>5</sup>A more rigorous definition of evaporation and evaporation mass will be presented later in the thesis.

## 1.4 Compact Objects as Dark Matter Probes

The main goal behind this work is to explore how compact objects can be used to probe a wide variety of dark matter interactions that terrestrial direct detection experiments are insensitive to. By compact objects, we are referring to Neutron Stars (NSs) and White Dwarfs (WDs), and not Black Holes that also fall into this category.

Compact objects offer a unique laboratory for studying dark matter and its interactions with the Standard Model in environments unachievable anywhere else in the Universe. They generate strong gravitational fields and are composed of incredibly dense matter, with NSs reaching super-nuclear densities in their central cores. The capture rate within these objects is therefore enhanced due to these properties, with benefits over solar capture including:

- **Gravitational focusing of the DM flux:** The strong gravitational field will increase the impact parameter of the infalling dark matter. This increases the effective size of the capturing body, increasing the flux of dark matter passing through it.
- **Relativistic Interaction Energies:** In general, the infalling dark matter will be accelerated to (semi-)relativistic velocities ( $\sim 0.2 - 0.7c$ ). Moreover, the stellar constituents will also have relativistic energies. As such, interactions that are momentum/velocity dependent will suffer far less suppression than in DD experiments.
- **Large Number of Targets:** The extremely high densities of these objects correspond to a considerable number of targets for scattering to occur. This allows these objects to probe very small scattering cross-sections, with NSs in particular expected to reach as low as  $\sim 10^{-45} \text{ cm}^2$ .
- **Forgot the last point....**

In the past, capture in NSs has been applied primarily in the context of sending gravitational collapse into black holes [104–110], and the modifications of NS merger rates as well as the gravitational wave signatures of these mergers [111–114]. Capture in WDs has also been considered, with a variety of different applications of the capture process [115–120].

In recent years, dark matter induced heating of NSs has reemerged as a potential detection frontier [121–128]. It was shown that dark matter could reheat old, isolated NSs in our local neighbourhood back up to temperatures that would cause them to radiate as blackbody peaked in the near-infrared. The aim is to locate the NSs with radio telescopes such as the Square-Kilometer-Array (SKA), and determine their age through their spindown rate. Once located, the star’s temperature

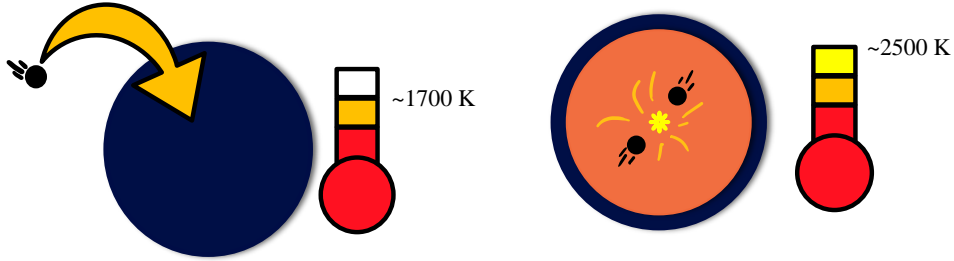


**Figure 1.6:** Illustration of DM-induced heating of compact objects. **Left:** kinetic heating due to DM scattering, raising the temperature to  $\sim 1700$  K. **Right:** Annihilation heating contributes an additional  $\sim 800$  K. This image is inspired by Ref. [121].

can be determined through observations from infrared telescopes such as the James Webb Space Telescope (JWST).

This heating occurs in two stages. The dark matter will first deposit its kinetic energy into the star through the scatterings required for capture and its subsequent thermalisation within the NS core, with this process called *kinetic heating*. If the dark matter can annihilate, it will deposit its mass energy, assuming the products are trapped within the star, termed *annihilation heating*. These processes are illustrated in Fig. 1.6. Assuming a NS in our local neighbourhood, i.e., within

In order to accurately determine the limits on dark matter interactions that such an observation could place, one first requires an accurate calculation of the capture rate. However, all previous calculations relied on the formalism set up by Gould for capture in the Sun, with only minor modifications made to accommodate the extreme nature of the compact objects.

Chapters ?? and ?? of this thesis are devoted to reformulating Gould’s capture formalism to account for the physics specific to compact objects in a self-consistent manner. These include a relativistic treatment of the kinematics, using General Relativity to calculate the correct dark matter flux passing through the star, and accounting for Pauli blocking of the final state target using Fermi-Dirac statistics for the stellar constituents. In addition, we incorporate the internal structure of these objects by calculating the radial profiles for the relevant microscopic quantities (e.g., chemical potentials and number densities) via the adoption of a realistic equation of state.

Further considerations are required when considering dark matter interactions with the baryonic matter inside NSs. Due to the high density of the NS interior, the baryonic matter undergoes strong interactions amongst themselves and should not be treated as a free Fermi gas. Instead, adopting an equation of state that accounts for these interactions is required. These interactions modify the mass of the baryons, leading them to obtain an effective mass smaller than their vacuum

mass. Furthermore, as we will see, the dark matter may interact with the baryons with momentum transfers on the order of 10 GeV. This is high enough that the dark matter will begin to resolve the internal structure of the baryon. To account for this, the momentum dependence of the baryon form factors that are typically neglected in direct detection and solar capture must be reintroduced.

This formalism is made in preparation for a thorough analysis of the timescales involved in the dark matter heating of compact objects. The energy deposited in both the kinetic and annihilation heating stages does not occur instantaneously, and the timescales involved in them need to be compared to the age of the star in question. We will define kinetic heating timescale as the time required for dark matter to deposit 99% of its initial kinetic energy into the star. For annihilation heating to occur, the dark matter must reach a state of capture-annihilation equilibrium within the stellar core. In standard calculations of this timescale, the dark matter must first become thermalised with the star. Only then can annihilations occur efficiently enough to heat the star.

We will work with the EFT operators in Table 1.1 that describe Dirac fermion dark matter interacting with Standard Model leptons. Each operator will be studied in isolation, i.e., by considering a Lagrangian that contains only one of the operators rather than a linear superposition of multiple. This way, we can analyse specific types of interactions independently, allowing us to take as model-independent an approach to phenomenology as possible.

# 2

## A Primer on Compact Objects

Within the cores of stars, there exists a delicate balance between the gravitational forces pulling the matter inward, and the outward pressure generated by the thermonuclear fusion of light elements. This process begins as is fused to form helium. Eventually, the hydrogen is depleted, allowing gravity to temporarily overcome the outward pressure leading to the core to begin contracting. As this occurs, the gravitational potential energy is converted to thermal energy and the core eventually becomes hot enough to facilitate helium burning.

This cycle can continue as heavier and heavier elements are formed within the ever-increasingly hot stellar core. Lighter stars cannot reach the temperature required to fuse light elements such as helium and carbon, ending the cycle there. If the star is heavy enough, iron will eventually be formed from the burning of silicon. As the fusion of iron nuclei is an endothermic process, it will not occur spontaneously, ending the cycle in heavy stars. Without a fuel source, the core will collapse under its own gravity, leading to the death of the star.

What comes after this collapse depends on the mass of the progenitor star. Very light stars,  $\lesssim 0.5M_{\odot}$ , have lifetimes much longer than the age of the universe, and so are uninteresting to our current discussion. Moderately heavy stars,  $1M_{\odot} \lesssim M_{\star} \lesssim 8M_{\odot}$ , will continue burning fuel until the outer layers of the star are dispersed as it expands, leaving a core comprised of helium, carbon and oxygen with small abundance of heavier elements. The core will begin to collapse until the Fermi degeneracy of the ultrarelativistic electrons is great enough to reestablish equilibrium, resulting in a White Dwarf (WD) [129].

Heavy stars,  $\gtrsim 8M_{\odot}$ , spectacularly end their lives in a type-II supernova event. This occurs when the core of the star exceeds the Chandrasekhar mass of  $1.4M_{\odot}$ , which cannot be supported by electron degeneracy pressure. The core itself will then collapse, leading to a shockwave that ejects the majority of the mass of the star.

All that will remain is an extremely dense core supported by neutron degeneracy pressure, a Neutron Star (NS) [130]. If the star was so massive that the gravitational forces overcome even the neutron degeneracy pressure, then the core collapses into a black hole.

These stellar corpses, white dwarfs, neutron stars, and black holes, are collectively known as compact objects. They have masses similar to or larger than the Sun, that is compressed into much smaller bodies with significantly larger surface gravities. These objects do not have a source of fuel, and spend the rest of their lives cooling through the emission of photons and neutrinos. For the remainder of this thesis, we will only be interested in white dwarfs and neutron stars and will collectively refer to these as compact objects, excluding black holes from this term.

This chapter is dedicated to discussing the aspects of the structure, composition, and observational status of these objects relevant to this work<sup>1</sup>.

## 2.1 Structure Equations from General Relativity

The highly dense matter comprising neutron stars and white dwarfs leads to extremely strong gravitational fields being produced by the stars. As such, modeling the structure of these objects falls into the domain of General Relativity (GR). Here we review the structure of static, spherically symmetric compact objects, following Refs. [131–133].

First, the static nature of the star means that the components of the metric are functions only of the spacial coordinates and not of time. Together with the assumption that the mass distribution of the star is spherically symmetric leads to a Schwarzschild-like metric of the form

$$ds^2 = -d\tau^2 = -B(r)dt^2 + A(r)dr^2 + r^2d\Omega^2, \quad (2.1)$$

with  $d\tau$  the proper time interval, and  $A(r)$ ,  $B(r)$  being functions only of the radial coordinate that are often written as

$$A(r) = e^{2\Lambda(r)}, \quad B(r) = e^{2\Phi(r)}. \quad (2.2)$$

These functions are subject to the condition that at distances far from the star,  $r \rightarrow \infty$ , space-time must become flat, which translates to the boundary conditions

$$\lim_{r \rightarrow \infty} A(r) = \lim_{r \rightarrow \infty} B(r) = 1. \quad (2.3)$$

---

<sup>1</sup>As this work is written from the perspective of a particle physicist, I wish to apologise to my astrophysics colleagues for what is to come.

The matter that comprises the star is modeled as a perfect fluid, meaning we are neglecting any shear stresses and energy transport within the star. Such a fluid is described by its pressure  $P(r)$ , density  $\rho(r)$ , and baryonic number density,  $n_b(r)$ , as well as the 4-velocity of the fluid  $u^\mu(r)$ . Being static, the only non-zero component of this velocity is the time component, which is fixed by the normalisation condition  $g_{\mu\nu}u^\mu u^\nu = -1$  to be  $u^t = 1/\sqrt{B(r)}$ . These quantities are used to construct the stress-energy tensor of the star, which takes the form

$$T^{\mu\nu} = (\rho + P)u^\mu u^\nu + Pg^{\mu\nu}. \quad (2.4)$$

The microphysics underlying the matter interactions are encoded in an equation of state (EoS) relating the various thermodynamic quantities. This is typically expressed by providing the pressure as a function of the density,  $P(\rho)$ . It is often more convenient to parameterise the EoS by the number density of baryons, and the entropy per baryon  $s$ , such that

$$P = P(n_b, s), \quad \rho = \rho(n_b, s). \quad (2.5)$$

The dependence on  $s$  turns out to be trivial in most scenarios involving compact objects, such as those considered here. The pressure in these stars arises from the degeneracy of the nucleons in NSs or the electrons in WDs, rather than from the thermal motion of the constituents as in main sequence stars. These thermal degrees of freedom will be frozen out at temperatures lower than the Fermi energy of the system, which is typically around  $E_F \sim 10$  MeV in NSs or  $\sim 1$  MeV in WDs, and correspond to temperatures of  $T_\star \sim 10^{11}$  K and  $\sim 10^{10}$  K respectively. As these objects are expected to cool well below these temperatures quickly after formation [134–136], the entropy can be taken to be zero throughout the star. This allows us to reduce the two-parameter EoS to a simpler one-parameter one,

$$P = P(n_b, s = 0) = P(n_b), \quad \rho = \rho(n_b, s = 0) = \rho(n_b). \quad (2.6)$$

The structure of the star is therefore dictated by the quantities  $A(r)$ ,  $B(r)$ ,  $P(r)$ ,  $\rho(r)$ , and  $n_b(r)$ . This system is determined by applying the Einstein field equations,  $G^{\mu\nu} = 8\pi T^{\mu\nu}$ , together with the energy-momentum conservation,  $T^{\mu\nu}_{;\nu} = 0$ , the EoS relations Eqs. 2.6, and the appropriate boundary conditions. The structure equations that come out of this analysis were first discovered concurrently by Tolman [137] and by Oppenheimer and Volkoff [138], and so are known as the TOV equations. They take the form

$$\frac{dP}{dr} = -\rho(r)c^2 \left[ 1 + \frac{P(r)}{\rho(r)c^2} \right] \frac{d\Phi}{dr}, \quad (2.7)$$

$$\frac{d\Phi}{dr} = \frac{GM(r)}{c^2 r^2} \left[ 1 + \frac{4\pi r^3 P(r)}{M(r)c^2} \right] \left[ 1 - \frac{2GM(r)}{c^2 r} \right]^{-1}, \quad (2.8)$$

$$\frac{dB}{dr} = 2B(r) \frac{d\Phi}{dr}, \quad (2.9)$$

where  $M(r)$  is related to the metric factor  $A(r)$  through

$$A(r) = \left[ 1 - \frac{GM(r)}{c^2 r} \right]^{-1}, \quad (2.10)$$

and is interpreted as the mass contained within a radius  $r$ . It obeys the mass equation

$$\frac{dM}{dr} = 4\pi r^2 \rho(r), \quad M(0) = 0, \quad (2.11)$$

that arises from the  $\mu = \nu = 0$  component of the Einstein field equations. These equations are the general relativistic versions of the hydrostatic equilibrium equations of regular stellar structure, with Eq. 2.7 reducing to the familiar

$$\frac{dP}{dr} = -\frac{GM(r)}{r^2} \rho(r), \quad (2.12)$$

in the Newtonian limit,  $GM(r)/c^2 r \ll 1$ .

The radius of the star,  $R_\star$ , is identified as the point at which the pressure and density vanish,  $P(R_\star) = \rho(R_\star) = 0$ . In the region outside the star,  $r > R_\star$ , the total mass remains constant at the mass of the star,  $M(r \geq R_\star) = M_\star$ , and so the only non-trivial structure functions in this region are the metric factors. Solving Eq. 2.9 with  $P(r) = 0$  and constant  $M(r)$  for  $B(r)$  becomes elementary while the result for  $A(r)$  is trivial, leaving us with

$$A(r) = \left[ 1 - \frac{GM_\star}{c^2 r} \right]^{-1}, \quad B(r) = 1 - \frac{GM_\star}{c^2 r}, \quad \text{for } r > R_\star, \quad (2.13)$$

and the metric reduces to the familiar Schwarzschild metric outside the star. Continuity of the metric at  $r = R_\star$  enforces a second boundary condition for  $B(r)$ ,

$$B(R_\star) = 1 - \frac{GM_\star}{c^2 R_\star}. \quad (2.14)$$

The final boundary condition required is the central pressure  $P(0) = P_c$ , or equivalently the central density/baryon number density. This is the only free parameter in the system and hence, for a given EoS, uniquely determines the stellar structure. All stars generated by an EoS can therefore be represented as a one-parameter sequence, typically represented as the mass-radius relation for the model.

Given all the above, we can write a simple recipe for constructing a model of a compact object:

1. Select an EoS to describe the constituent matter.

2. Specify the central pressure of the star,  $P_c$ .
3. Integrate the coupled system of differential equations 2.7, 2.8, 2.11 from the centre of the star outward until the pressure vanishes.
4. Use the boundary condition Eq. 2.14 to normalise the metric function  $B(r)$ .

In general, additional quantities will be present in the EoS, such as chemical potentials and the speed of sound, that may be subject to additional constraints. These quantities will need to be calculated at each step of the integration alongside the other structure functions.

## 2.2 White Dwarfs

The fate of main sequence stars of mass below  $M_\star \lesssim 8M_\odot$  is to end their lives as a white dwarf. Consequently, these compact stellar remnants, which are supported against gravitational collapse by electron degeneracy pressure, are the most abundant stars in the Galaxy ( $\gtrsim 90\%$ ). They are born at very high temperatures and cool down over billions of years. Observations of the coldest WDs therefore contain information on the star formation history of the Galaxy.

The vast majority of observed WDs are composed primarily of carbon and oxygen, plus small traces of elements heavier than helium. At the extremely high densities found in WDs,  $\rho_\star \sim 10^6 - 10^{10} \text{ g cm}^{-3}$ , electrons are strongly degenerate and determine the WD equation of state (EoS) and internal structure. The stellar core resembles a Coulomb lattice of ions surrounded by the degenerate electron gas, implying that the WD core is isothermal and a very good thermal conductor. The degenerate core is enclosed by a thin envelope that accounts for  $\lesssim 1\%$  of the total mass [139].

The outer layers form an atmosphere that is rich in lighter elements such as hydrogen or helium, where the exact composition depends on the evolution of the WD progenitor and changes as the WD cools. This atmosphere is non-degenerate and extremely opaque to radiation, with an EoS that is subject to finite temperature effects. We limit our discussion to the core region of the WD that accounts for the vast majority of its mass.

### 2.2.1 The FMT Equation of State

In the limit of zero temperature, the simplest way to obtain the WD EoS is to assume an ideal Fermi gas of degenerate electrons, for a WD that is primarily composed of a single element. Corrections to the non-interacting electron picture

were introduced early by Salpeter [140]. By introducing the Wigner-Seitz (WS) cell approximation and assuming point-like nuclei, Salpeter obtained an analytical EoS that accounts for interactions between electrons and ions as well as other Coulomb corrections. These corrections, in general, depend on the chemical composition of the star.

More recently, it has been shown that the treatment of matter at high pressures presented by Feynman, Metropolis and Teller [141] can be extended to consistently take into account weak interactions and relativistic effects [142, 143], and incorporates Coulomb corrections in a more natural manner than the Salpeter EoS. The resulting Feynman-Metropolis-Teller (FMT) EoS is obtained by considering a relativistic Thomas-Fermi model within Wigner-Seitz cells of radius  $R_{\text{WS}}$ . For degenerate, relativistic, electrons, the equilibrium condition is that the Fermi energy,  $E_e^F$ , is constant within the cell,

$$E_e^F = \sqrt{(p_e^F)^2 + m_e^2} - m_e - eV(r) = \text{constant}, \quad (2.15)$$

where  $V(r)$  is the Coulomb potential inside the cell,  $p_e^F$  is the electron Fermi momentum,  $m_e$  is the electron mass and  $e$  is the electric charge. To obtain an integrable solution for the energy density near the origin, it is necessary to introduce a finite size for the nucleus, with radius  $R_c = \Delta\lambda_\pi Z^{1/3}$ , where  $\lambda_\pi$  is the pion Compton wavelength,  $\Delta \approx (r_0/\lambda_\pi)(A/Z)^{1/3}$ ,  $Z$  is the proton number,  $A$  is the atomic mass, and  $r_0$  is an empirical constant  $\sim 1.2$  fm. The proton and electron number densities inside the cell are then given by

$$n_p = \frac{(p_p^F)^3}{3\pi^2} = \frac{3Z}{4\pi R_c^3} \theta(R_c - r) = \frac{3}{4\pi} \left( \frac{1}{\Delta\lambda_\pi} \right)^3 \theta(R_c - r), \quad (2.16)$$

$$n_e = \frac{(p_e^F)^3}{3\pi^2} = \frac{1}{3\pi^2} \left[ \hat{V}^2(r) + 2m_e \hat{V}(r) \right]^{3/2}, \quad (2.17)$$

$$\hat{V}(r) = eV(r) + E_e^F. \quad (2.18)$$

The Coulomb potential satisfies the Poisson equation

$$\nabla^2 V(r) = -4\pi e[n_p(r) - n_e(r)], \quad (2.19)$$

with requiring global charge neutrality of the cell enforcing the boundary conditions

$$\left. \frac{dV}{dr} \right|_{r=R_{\text{WS}}} = V(R_{\text{WS}}) = 0. \quad (2.20)$$

In practice, it is beneficial to work with dimensionless quantities, and so we define  $x = r/\lambda_\pi$  and  $\chi(r) = r\hat{V}(r)$ , such that  $x_c = R_c/\lambda_\pi$  and  $x_{\text{WS}} = R_{\text{WS}}/\lambda_\pi$ . Using

these expressions results in the relativistic Thomas-Fermi equation

$$\frac{1}{3x} \frac{d^2\chi}{dx^2} = -\frac{\alpha_{\text{EM}}}{\Delta^3} \theta(x_c - x) + \frac{4\alpha_{\text{EM}}}{9\pi} \left[ \frac{\chi^2(x)}{x^2} + 2 \frac{m_e}{m_\pi} \frac{\chi(x)}{x} \right]^{3/2}, \quad (2.21)$$

with the boundary conditions

$$\chi(0) = 0, \quad \left. \frac{d\chi}{dx} \right|_{x_{\text{WS}}} = \frac{\chi(x_{\text{WS}})}{x_{\text{WS}}}. \quad (2.22)$$

By solving these equations, we can obtain the relevant thermodynamic quantities, namely the electron and proton number densities, electron chemical potential, and the energy and pressure of the cell. The electron chemical potential is obtained by evaluating Eq. 2.15 at the cell radius, noting that the Coulomb potential must vanish there, which results in the usual expression<sup>2</sup>

$$\varepsilon_{F,e} = \sqrt{(p_e^F)^2 + m_e^2} - m_e. \quad (2.23)$$

The energy and pressure of the cell can then be obtained following the analysis presented in ref. [143]. The cell energy gains contributions from the nuclear mass, electron kinetic energy, and Coulomb interactions, such that

$$E_{\text{tot}} = M_N + E_k + E_C, \quad (2.24)$$

$$E_k = \int_0^{R_{\text{WS}}} 4\pi r^2 [\mathcal{E}_e(r) - m_e n_e(r)] dr, \quad (2.25)$$

$$E_C = \frac{1}{2} \int_{R_c}^{R_{\text{WS}}} 4\pi r^2 e [n_p(r) - n_e(r)] V(r) dr, \quad (2.26)$$

where

$$\mathcal{E}_e(r) = \frac{1}{\pi^2} \int_0^{p_e^F} p^2 \sqrt{p^2 + m_e^2} dp, \quad (2.27)$$

is the electron energy density, and  $M_N$  is the mass of the nucleus. The energy density of the cell is then simply

$$\rho_{\text{WS}} = \frac{E_{\text{tot}}}{V_{\text{WS}}}, \quad (2.28)$$

where  $V_{\text{WS}} = 4\pi R_{\text{WS}}/3$  is the volume of the WS cell. The only contribution to the internal cell pressure comes from the electrons,

$$P_e(r) = \frac{1}{3\pi^2} \int_0^{p_e^F} \frac{p^4}{\sqrt{p^2 + m_e^2}} dp, \quad (2.29)$$

---

<sup>2</sup>We use the symbol  $\varepsilon_{F,i}$  to represent the chemical potential minus the mass of a particle species  $i$ , reserving  $\mu_{F,i}$  for the full chemical potential.

<b>EoS</b>	<b>WD<sub>1</sub></b>	<b>WD<sub>2</sub></b>	<b>WD<sub>3</sub></b>	<b>WD<sub>4</sub></b>
$\rho_c$ [g cm <sup>-3</sup> ]	$1.47 \times 10^6$	$3.84 \times 10^7$	$3.13 \times 10^8$	$2.31 \times 10^{10}$
$M_\star$ [ $M_\odot$ ]	0.440	1.000	1.252	1.384
$R_\star$ [km]	$9.39 \times 10^3$	$5.38 \times 10^3$	$3.29 \times 10^3$	$1.25 \times 10^3$
$v_{\text{esc}}(R_\star)$ [km/s]	$3.72 \times 10^3$	$7.03 \times 10^3$	$1.01 \times 10^4$	$1.71 \times 10^4$

**Table 2.1:** Four configurations for white dwarfs composed of carbon, with an FMT EoS. Shown are the central densities,  $\rho_c$ , stellar mass  $M_\star$  and radius  $R_\star$ , and escape velocity at the edge of the WD,  $v_{\text{esc}}$ .

with the total pressure of the cell being  $P_{\text{tot}} = P_e(R_{\text{WS}})$ . Finally, the EoS is then obtained by solving Eq. 2.21 for various cell radii, yielding a relation between  $E_{\text{tot}}(R_{\text{WS}})$  and  $P_{\text{tot}}(R_{\text{WS}})$  parameterised by the radius of the Wigner-Seitz cell.

Different WD configurations can be obtained, assuming a non-rotating spherically symmetric star, by solving the Tolman-Oppenheimer-Volkoff (TOV) equations [137, 138] coupled to the FMT EoS with different initial conditions for the pressure at the centre of the star. In Fig. 2.1 we show radial profiles for  $n_e$  (top left),  $\varepsilon_{F,e}$  (top right), and escape velocity  $v_{\text{esc}}$  (bottom) for the carbon WDs in Table 2.1. Note that the difference in radius between the lightest and heaviest WD in Table 2.1 spans almost one order of magnitude, while the electron number densities in the core can vary up to 4 orders of magnitude (see top left panel). As expected, electrons are more degenerate in more compact WDs and become relativistic (see top right panel). The escape velocity can reach  $\mathcal{O}(0.1 c)$  at the interior of the most compact WDs, while for very low mass WDs it can be as low as  $\sim 0.003 c$ .

The mass-radius relations obtained from a zero-temperature EoS begin to deviate from observations for low-mass WDs. To address this discrepancy, finite temperature effects can be introduced to the EoS [144]. The extension to finite temperatures is made by reintroducing the temperature dependence in the Fermi-Dirac distributions. Now, the electron chemical potential is no longer simply the Fermi energy of the system due to thermal corrections. Define the finite temperature Fermi-Dirac integrals of degree  $s$  as

$$F_s(\eta, \beta) = \int_0^\infty \frac{t^s \sqrt{1 + (\beta/2)t}}{1 + e^{t-\eta}} dt, \quad (2.30)$$

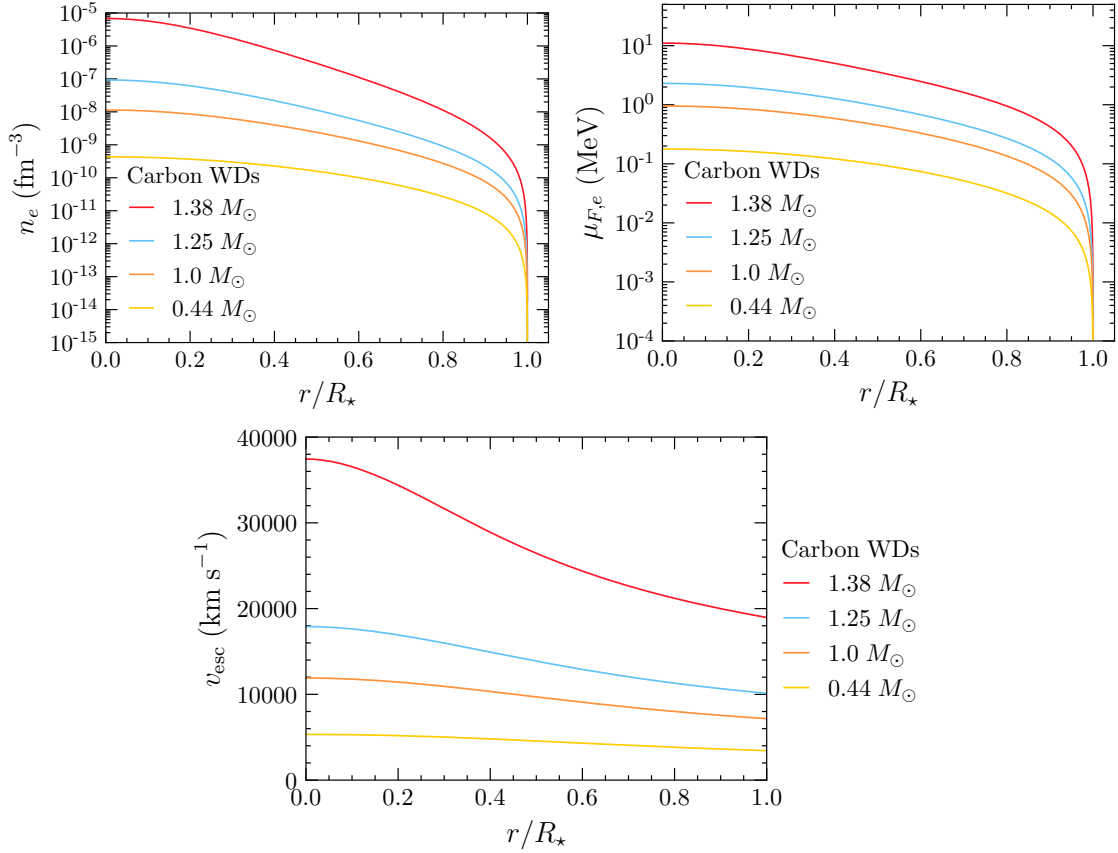


**Figure 2.1:** Electron number density (top left), chemical potential (top right), and escape velocity (bottom) radial profiles for the carbon WDs with FMT EoS in Table 2.1. The radial distance of each profile has been normalised to the radius of the star.

where we define the dimensionless quantities

$$t = \frac{E_e - m_e}{T_\star}, \quad (2.31)$$

$$\eta = \frac{\varepsilon_{F,e}}{T_\star}, \quad (2.32)$$

$$\beta = \frac{T_\star}{m_e}, \quad (2.33)$$

for a star at temperature  $T_\star$ . The Thomas-Fermi equilibrium condition within the WS cell is now given by

$$\varepsilon_{F,e}(r) - eV(r) = T_\star\eta(r) - eV(r) = \text{constant}, \quad (2.34)$$

with the Coulomb potential vanishing at the boundary of the cell as before. We

now make the change of variables into the dimensionless quantities  $\chi/r = \varepsilon_{F,e}/(\hbar c)$  and  $x = x/x_{\text{WS}}$  so that the Poisson equation 2.19 becomes

$$\frac{d^2\chi}{dx^2} = -4\pi\alpha_{\text{EM}}x \left( \frac{3}{4\pi\Delta^3} \theta(x_c - x) - \frac{\sqrt{2}}{\pi^2} \left( \frac{m_e}{m_\pi} \right)^2 [F_{1/2}(\eta, \beta) + \beta F_{3/2}(\eta, \beta)] \right), \quad (2.35)$$

$$\eta(x) = \left( \frac{1}{\lambda_\pi T_\star} \right) \frac{\chi(x)}{x}, \quad (2.36)$$

with the same boundary conditions as in Eq. 2.22.

The total energy of the cell remains very similar to the zero-temperature case, the main differences being it gains a contribution from the thermal motion of the nucleus,

$$E_{\text{th}} = \frac{3}{2}T_\star, \quad (2.37)$$

and that the electron energy density is now given by

$$\mathcal{E}_e = m_e n_e + \frac{\sqrt{2}}{\pi^2} m_e^4 \beta^{5/2} [F_{3/2}(\eta, \beta) + \beta F_{5/2}(\eta, \beta)]. \quad (2.38)$$

The pressure of the cell will now gain contributions from the motion of the nucleus as well as the electron, such that the total pressure is

$$P_{\text{tot}} = P_N + P_e, \quad (2.39)$$

$$P_N = \frac{2}{3} \frac{E_{\text{th}}}{V_{\text{WS}}} = \frac{T_\star}{V_{\text{WS}}}, \quad (2.40)$$

$$P_e = \frac{2^{3/2}}{3\pi} m_e^4 \beta^{5/2} [F_{3/2}(\eta(x_{\text{WS}}), \beta) + \beta F_{5/2}(\eta(x_{\text{WS}}), \beta)]. \quad (2.41)$$

In Fig. 2.2 we show the Mass-Radius relations obtained from the zero temperature FMT EoS together with several finite temperature configurations. As can be seen, the deviations from the zero temperature approximation begin at rather high temperatures,  $T_\star \gtrsim 10^7$  K, for masses  $\lesssim 0.6M_\odot$ . Additionally, we show a random selection of 20,000 WDs presented in the Gaia early data release 2 (EDR2) report [145] as the yellow-red dots. The colour of the dot represents the internal temperature of the corresponding WD. The core temperature must be determined from the observed effective surface temperature of the star<sup>3</sup>, with the relation between the two depending on the composition of the WD atmosphere. To obtain

---

<sup>3</sup>The effective temperature is the temperature that characterises the surface of the star. Assuming that WDs are perfect blackbody emitters, the luminosity will be  $L_\gamma = 4\pi\sigma_{SB} R_\star^2 T_{\text{eff}}^4$ , where  $\sigma_{SB}$  is the Stefan–Boltzmann constant.

the central temperature from the reported effective temperatures, we use the WD cooling sequences generated in Ref. [136]<sup>4</sup> assuming a thin hydrogen atmosphere. In general, there is good agreement between the mass-radius relations derived from the finite temperature FMT EoS and the observed internal temperatures of the WDs.

Given the non-linear nature of the differential equations that describe the FMT EoS (both at zero and finite temperatures), solving the system is a numerically challenging task. As there are no publicly available resources to help solve these systems, a significant amount of time was put into solving this problem. As such, we have outlined in Appendix **ADD THIS APPENDIX** the method employed in numerically solving the differential equations.

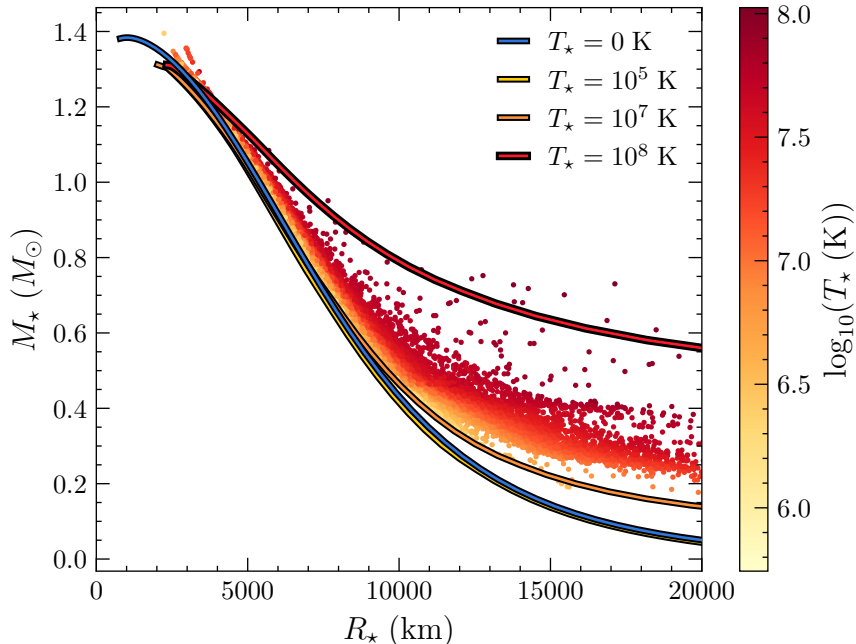


**Figure 2.2:** Mass-Radius relation of WDs calculated from the FMT EoS in the zero temperature approximation (dark blue), at  $10^5$  K (yellow),  $10^7$  K (orange), and  $10^8$  K (red), together with observed WDs from Gaia EDR2 observations [145] (light blue dots).

---

<sup>4</sup>The cooling sequence data can be obtained from [this cite](#).

### 2.2.2 Observational Status

The rate at which the energy of the WD core is radiated away is determined by the outer non-degenerate layers of the atmosphere. Spectroscopic observations shed light on the composition of these layers and can be used to classify WDs in terms of  $\sim$  six spectral types. Most of the observed WDs lie in the DA (hydrogen-rich) and DB (helium-rich) categories. Note that as WDs slowly cool, they undergo spectral evolution. There is a well-defined relation between their luminosity and age (cooling time) that, together with recent breakthroughs in theory and observations, allow us to estimate the age of the stars within the solar neighbourhood and to date the nearest star clusters [146–150].

Over the past few decades, WDs have been extensively observed using photometry and spectroscopy. Most of the WDs have been discovered by large area surveys, such as the Sloan Digital Sky Survey (SDSS) [151]. However, these local samples are dominated by young WDs with relatively high effective temperatures ( $T_{\text{eff}} \gtrsim 10^4$  K) [152–156]. Recently, the local volume sample of nearby stars within  $\sim 100$  pc has been catalogued by the Gaia spacecraft [157, 158], an astrometric mission. New WD candidates have been identified [145], followed by dedicated spectroscopic observations [159, 160], increasing the local sample of cool WDs ( $T_{\text{eff}} \lesssim 5000$  K).

On the other hand, globular clusters (GCs) are the oldest known stellar systems in the Galaxy. Among them is Messier 4 (M4), also classified as NGC 6121, which is the closest globular cluster to Earth being  $\sim 1.9$  kpc away [161–163]. The age of M4, 11.6 Gyr, has been estimated using observations of faint cold WDs with the Hubble Space Telescope (HST) [146, 148]. This HST data, corrected for reddening and extinction, was converted into luminosities and effective temperatures in ref. [117]. From these calculations, it is possible to infer WD radii and their corresponding masses by assuming a mass-radius relation.

## 2.3 Neutron Stars

Being the end product of massive,  $\gtrsim 8M_{\odot}$ , stars, there are significantly fewer NSs than the WDs discussed above. As their name suggests, they are composed primarily of neutrons, which provide the degeneracy pressure required to prevent the gravitational collapse of the star. The internal structure of an NS is significantly more complicated than that of a WD. Broadly speaking, an NS can be divided into five main regions. We give an overview of the important features of each of these regions, and point the reader to Refs. [164–171] for more indepth discussions. Working from the outside in, these regions are:

## Atmosphere

The atmosphere is an extremely thin layer of plasma that makes up less than 1% of the NS mass. However, it plays an extremely important role as the observed spectrum radiation emitted by the star must pass through this region [165, 166].

## Outer Crust

The outer crust is the thin layer of ionized Iron-56 nuclei that extends down until the density reaches the neutron drip point,  $\rho_\star = \rho_{\text{ND}} \sim 4.3 \times 10^{11} \text{ g cm}^{-3}$ . This is the density at which neutrons begin to drip from the nuclei as their chemical potentials approach zero. The ionized electrons form a non-relativistic but degenerate gas, with their chemical potentials increasing as the density increases. This leads to the “neutronisation” of the nuclei as the beta-capture of electrons by protons increases.

## Inner Crust

The density within the inner crust spans the range between  $\rho_{\text{ND}} \lesssim \rho_\star \lesssim 0.5\rho_0$ , with  $\rho_0 \sim 2.8 \times 10^{14} \text{ g cm}^{-3}$  the nuclear saturation density (i.e. the density of nuclear matter) [165, 166, 172]. Here, the neutrons that have dripped from the nuclei will potentially form a superfluid. Towards the crust-core boundary, the nuclear lattice begins taking on interesting topological structures that are distinguished by the configuration of the voids in the lattice. These are known as the so-called *pasta phases* [173–175] of nuclear matter:

- 2D void cylinders creating spaghetti structures of nuclei
- Planar voids with slabs of nuclei forming lasagna sheets
- 3D cylindrical voids leading to thin 2D cylinders of nuclear ziti
- 3D spherical voids enclosed by ravioli
- 2D circular voids in sheets of Swiss cheese

Eventually, towards the crust-core interface the nuclear matter transitions into a uniform medium<sup>5</sup>.

---

<sup>5</sup>The nuclear minestrone, if you will

## Outer Core

Once densities go above  $0.5\rho_0$ , the nuclear clusters will dissolve into a homogenous fluid that is composed of neutrons, protons, electrons, and muons known as *npeu* matter. The relative abundances of the species,  $Y_i = n_i/n_b$ , are dictated by the conditions of electrical neutrality and beta-equilibrium. Charge neutrality dictates that the abundances of the charged particles obeys

$$Y_p = Y_e + Y_\mu, \quad (2.42)$$

while beta-equilibrium refers to the balance between the weak decays of neutrons and the electron/muon capture by the protons,



with  $\ell = e, \mu$ . Muons will begin to replace electrons in these reactions once the electron chemical potential exceeds the mass of the muon,  $\mu_{F,e} \gtrsim m_\mu = 105.7 \text{ MeV}$ . As neutrinos are assumed to escape the NS once produced, the relation between the chemical potential of the leptons is simply

$$\mu_{F,e} = \mu_{F,\mu}, \quad (2.45)$$

on the chemical potentials. The outer core region ends once the density reaches  $\rho_\star \sim 2\rho_0$ , and we transition into the inner core.

## Inner Core

The densities within the inner cores of NSs extend between  $2\rho_0 \lesssim \rho_\star \lesssim (10 - 15)\rho_0$  and are hence a mystery to this day. As the density exceeds well above any material that can be produced in a laboratory, the exact composition of this region is unknown and depends on the equation of state one adopts to describe it. Some of the more well-known candidates are

- The appearance of hyperonic matter, i.e. nucleons containing a valence strange quark. These appear once the neutron chemical potential equals the  $\Lambda^0$  hyperon, with the  $\Xi^-$  appearing once its chemical potential equals the sum of the chemical potentials of the neutrons and electrons [167, 176].
- Pion/Kaon condensates. These are Bose-Einstein condensates of pion/kaon-like excitations [177–182].
- A quark-gluon plasma comprised of deconfined  $u$ ,  $d$  and  $s$  quarks and gluons [183–185].

### 2.3.1 Observational Status

Unlike the WDs discussed above, there are much fewer NS observations that constrain the EoS. However, recent years have seen significant strides in furthering our understanding of matter at super-nuclear densities, both from a theory and observational standpoint. On the theoretical side, these advances come from developments in chiral EFT allowing more detailed modelling of nuclear interactions [186–188], while the observational data has been bolstered thanks to the onset of gravitational wave astronomy due to the LIGO-VIRGO experiment [189–191] and the launch of the Neutron star Interior Composition Explorer (NICER) X-ray timing instrument.

Ultimately, what is needed to further constrain the NS EoS are more precise observations of NS masses and radii, which can be obtained from various observational techniques. NS masses have historically been much easier to measure than their radii. In particular, masses of NSs in binary systems can be precisely determined as the underlying gravitational theories are well-understood today [169, 170, 192–194]. The radii must be determined by assuming the NSs emit a blackbody spectrum, however, this method is only reliable for cool NSs where the atmospheric models are well understood [194].

The NICER experiment can provide much more precise measurements of NS radii than previous methods. This is achieved by measuring the X-ray pulse profiles of pulsars, that are sensitive to how light bends around the star. This provides information on the compactness of the star,  $GM_\star/R_\star c^2$ , that can be used to determine  $M_\star$  and  $R_\star$  given that the mass can usually be determined through other means. The heaviest NS observed to date, the millisecond pulsar PSR J0740+6620 [195, 196], had its mass determined by measuring the relativistic Shapiro time delay [197]<sup>6</sup> of the radio signal, allowing the radius to be obtained once the compactness was measured [198]. Refined analyses result in a mass of  $2.08 \pm 0.07 M_\odot$  [199] and a radius of  $12.39^{+1.30}_{-0.98}$  km [196] or  $13.71^{+2.61}_{-1.50}$  km [195] at 68% confidence levels.

Gravitational wave astronomy offers an alternative and independent determination of NS masses and radii to the electromagnetic observations above. The best candidate events for this analysis are NS binary mergers, though these are expected to be an uncommon occurrence. As the NSs inspiral toward each other, they will begin to deform due to the tidal forces they induce on one another [200]. This deformation will alter the waveform observed at the detectors, with the shift in the phase of the waveform depending on the mass ratio,  $q = M_2/M_1 < 1$ , the chirp mass of the system,  $\mathcal{M}_{\text{chirp}} = (M_1 M_2)^{3/5} / (M_1 + M_2)^{1/5}$ , and a combination of the tidal deformabilities,  $\tilde{\Lambda}$ . The latter refers to how susceptible the star is to deformation due to tidal forces acting upon it, with larger values corresponding to less compact objects. Comparing the observed waveform to that determined from

---

<sup>6</sup>This refers to the time it takes for light to move out of a gravitational well taking longer than the naive Newtonian prediction due to the curvature of space-time.

precise numerical simulations allows constraints to be placed on these parameters, and ultimately on the masses and radii of the merging NSs.

Furthermore, the electromagnetic emission from the remnant object provides information about the maximum mass an NS can achieve. If the mass of the remnant object is too large, it will collapse into a black hole, and it is highly unlikely that a gamma-ray burst will occur. If the remnant does not immediately collapse, then its mass and how it is rotating determines whether it will be hydrodynamically stable, unstable, or metastable against gravitational collapse. A remnant that undergoes differential rotation<sup>7</sup> can support heavier masses than one that is uniformly rotating. Hence, the afterglow spectrum can inform us as to how the star is rotating. Comparing the maximum mass supported by this rotation to the initial mass after inspiral yields an upper bound on the maximum NS mass achievable.

To date, the only confirmed NS-NS merger is the merger event GW170817 observed at LIGO-VIRGO in 2017 [190, 191], with the gamma-ray burst counterpart signal observed at the Fermi Gamma-ray Burst Monitor and INTEGRAL satellite [189]. These observations led to the constraint that the radius of a  $1.4M_{\odot}$  NS has an upper bound of  $R_{1.4} < 13.3$  km [201, 202], and that the maximum NS mass must be  $M_{\text{NS,MAX}} < 2.18M_{\odot}$  [189].

### 2.3.2 Neutron Star Equations of State

Given the scarce constraints that have been placed on the NS mass-radius relation, there are numerous equations of state in the literature that can be used to incorporate the internal structure into our calculations. In this work, we adopt two different EoSs, which we detail here.

#### The Brussels-Montreal EoS

The first family of EoSs adopted in this work are based on the Brussels-Montreal (BSk) energy density functionals [203–208], for cold, non-accreting NSs. In these models, the density-dependent nucleon interactions are accounted for via a mean-field approximation in either the Hartree-Fock (HF) or Hartree-Fock-Bogoliubov (HFB) formalism<sup>8</sup>, through effective Skyrme type forces [209, 210]. The BSk EoS family are unified EoSs, meaning they describe all the regions of the NS interior using the single effective Hamiltonian. Furthermore, the authors provide public FORTRAN subroutines that implement fits to the EoS quantities such as the pressure

---

<sup>7</sup>This is when components of the star at different latitudes have different angular velocities.

<sup>8</sup>The HF method accounts for the energy associated with nucleon pairings, while the HFB method neglects this contribution.

<b>EoS</b>	<b>BSk24-1</b>	<b>BSk24-2</b>	<b>BSk24-3</b>	<b>BSk24-4</b>
$\rho_c$ [g cm $^{-3}$ ]	$5.94 \times 10^{14}$	$7.76 \times 10^{14}$	$1.04 \times 10^{15}$	$1.42 \times 10^{15}$
$M_\star$ [ $M_\odot$ ]	1.000	1.500	1.900	2.160
$R_\star$ [km]	12.215	12.593	12.419	11.965
$B(R_\star)$	0.763	0.648	0.548	0.467
$c_s(0)$ [c]	0.511	0.628	0.734	0.835

**Table 2.2:** Benchmark NSs, for four different configurations of the equations of state (EoS) for cold non-accreting neutron stars with Brussels–Montreal functionals BSk24 [208]. EoS configurations are determined by the central mass-energy density  $\rho_c$ .

and density as functions of the baryon number density, allowing straightforward implementation of the EoS.

The authors provide these fits to seven configurations of the BSk EoS, labeled BSk19-26. Of these, the older BSk19-21 functionals were fitted to older atomic mass data that has since been updated in the newer models, BSk22-26. The mass-radius relation predicted by a selection of these models is shown in Fig. 2.4 by the blue lines. Missing are the BSk20 and 21 models, as they give very similar results to the 26 and 24 models respectively. The BSk19 EoS is partially ruled out from the lower bound on NS radii obtained from the electromagnetic counterpart of the GW170817 event [211], while BSk22 is ruled out from constraints on the tidal deformability from the same event [212]. Additionally, BSk22 does not support the presence of direct Urca<sup>9</sup> processes in NSs described by this EoS. These processes are required to explain observations of a small population of NSs that have cooled to temperatures below those predicted by the “minimal cooling paradigm” [213, 214]. On the other hand, the BSk26 functional predicts that all stable NSs will support direct Urac processes. This goes against the current observational evidence that a majority of NSs are well modeled by the minimal cooling paradigm, ruling the EoS out. Of the remaining two models, BSk24 and 25, we choose to adopt BSk24 as it gives slightly better fits to NS mass data than that of BSk25.

We use the BSk24 EoS to generate four benchmark NSs with masses of 1, 1.5, 1.9 and 2.16  $M_\odot$ , with the central density  $\rho_c$ , stellar mass, radius, metric factor  $B(R_\star)$  and central speed of sound  $c_s(0)$  in Table 2.2. Radial profiles of the baryon number density  $n_b(r)$ , metric factor  $B(r)$ , neutron chemical potential  $\varepsilon_{F,n}(r)$ , and neutron abundance  $Y_n(r)$ , are shown in Fig. 2.3.

While BSk24 and 25 lie well within current observational constraints, they are minimal models in that they only account for  $npe\mu$  matter, and do not incorpo-

<sup>9</sup>This is another name given to the reactions in Eqs. 2.43, 2.44

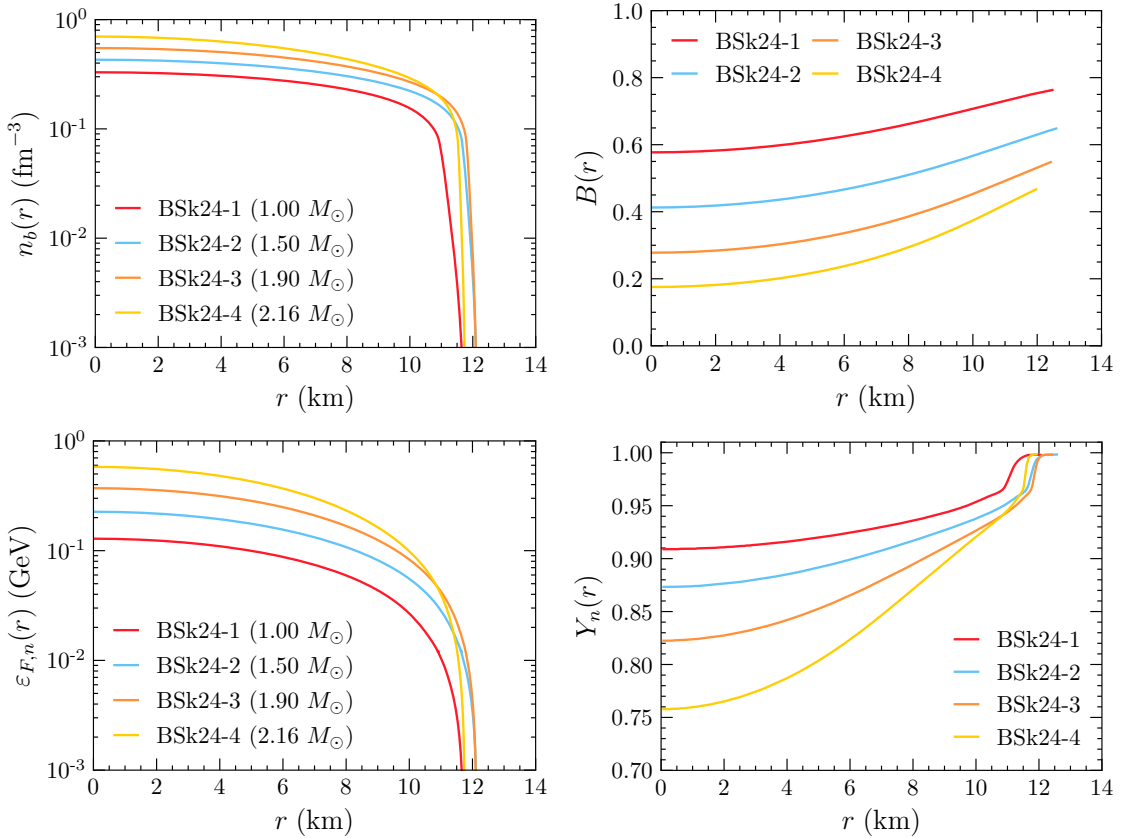


**Figure 2.3:** Radial profiles of the baryon number density (top left), metric factor  $B(r)$  (top right), neutron chemical potential (bottom left), and neutron abundance (bottom right) for the four benchmark NS of the BSk24 EoS in Table 2.2.

rate any exotic species within the NS core. This is problematic as it is highly likely that hyperonic matter will appear in the cores of NS heavier than  $\sim 1.7 M_\odot$ . Additionally, the Skyrme forces that describe the nuclear interaction are treated non-relativistically, while the nucleons in heavier stars can become semi-relativistic. To address these concerns, later works [215, 216] adopted the Quark-Meson Coupling (QMC) EoS.

### The Quark-Meson Coupling EoS

The second EoS adopted is based on the QMC model of Refs. [217–220], in which baryons are described as bags of three valence quarks, with the bags themselves modeled by the MIT bag model [221]. The interactions among the baryons are described by the exchange of mesons between the valence non-strange quarks and

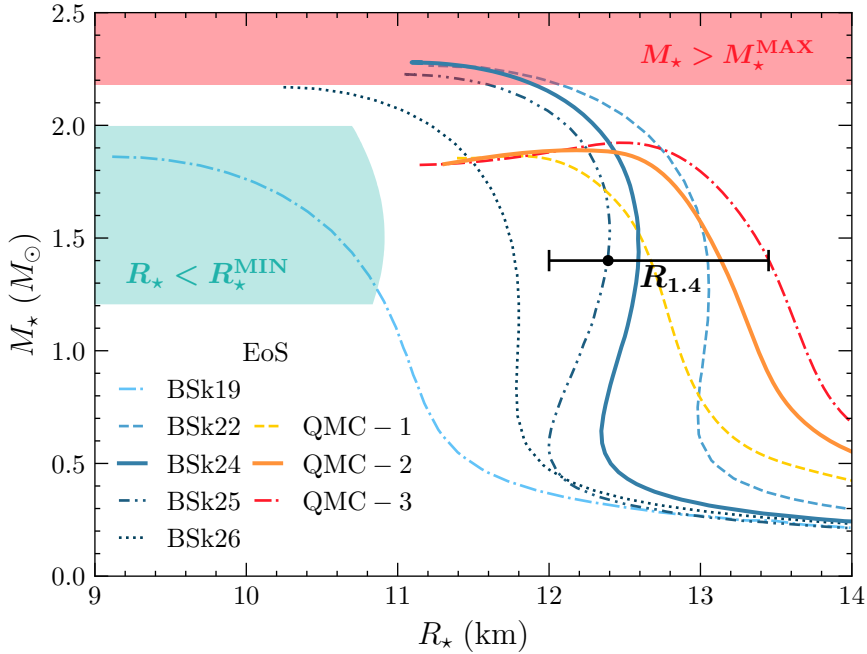


**Figure 2.4:** Neutron Star Mass-Radius relation predicted by the BSk (blue lines) and QMC (red lines) EoSs. Constraints obtained from the gravitational wave event GW170817 are shown as the shaded regions, with the lower bound on the radius in turquoise, and the maximum NS mass possible in red. The line band labeled  $R_{1.4}$  indicates the constraints on the radius of a  $1.4 M_\odot$  NS.

are formulated within a relativistic mean-field Lagrangian. The exchange of the vector mesons acts as an overall shift to the energy of the baryons<sup>10</sup>. The scalar mean fields play a significantly more important role, modifying the effective mass of the baryons. The scalar (and also vector) couplings are density-dependent, leading to an effective mass of the baryons that varies throughout the NS. The density dependence of these couplings is equivalent to including repulsive three-body forces between the baryons and arises naturally in the QMC model through the in-medium modification of the baryonic structure [222, 223]. Additional details on the energy density and couplings of the QMC model adopted in this work are given in Appendix ADD APPENDIX

The mass-radius relation of three different configurations of the QMC EoS, namely three different choices of the isovector coupling constant, are shown as the red lines in Fig. 2.4, obtained from Ref. [224]. Of these, QMCb lies within the constraints on the radius of a  $1.4 M_\odot$  NS from GW170817, and can produce an NS

<sup>10</sup>A simple analogy for this is how the energy of an electron in an electromagnetic field is due to the exchange of photons, which are vector fields.

EoS	QMC-1	QMC-2	QMC-3	QMC-4
$n_B^c$ [fm $^{-3}$ ]	0.325	0.447	0.540	0.872
$M_\star$ [ $M_\odot$ ]	1.000	1.500	1.750	1.900
$R_\star$ [km]	13.044	12.847	12.611	12.109
$B(R_\star)$	0.772	0.653	0.588	0.535

**Table 2.3:** Benchmark NSs for four different configurations of the QMC equation of state. EoS configurations are determined by the central number density  $n_B^c$ .

of mass  $1.908 \pm 0.016 M_\odot$ , the currently preferred mass of PSR J1614-2230 obtained by the NANOGrav collaboration [225]<sup>11</sup>.

The QMCb EoS data was provided by the authors of Ref. [224] for use in this work and will be referred to as simply the QMC EoS from here on. From this, we calculate the internal structure of four benchmark NSs, similar to Table 2.2 with the central baryon density replacing the central density and the speed of sound omitted. The top four plots in Fig. 2.5 show the radial profiles for the number densities of the neutrons and protons for each configuration on the left, with their effective masses shown on the right. The bottom two plots of the same figure show the number densities for each species within the heaviest star on the left, including leptons in dashed lines, with the effective masses for each of the baryons on the right. The replacement of high-momentum neutrons with low-momentum hyperons is clearly seen in the bottom left plot, as the neutron number density dips towards the centre of the massive star. As the densities are high enough for the charged hyperon  $\Xi^-$  to appear, the abundance of leptons decreases due to the requirement of charge neutrality, also seen in this plot.

---

<sup>11</sup>As mentioned above, the current heaviest NS has a mass of  $2.08 \pm 0.07 M_\odot$  though the implications of this on the QMC EoS are beyond the scope of this work.

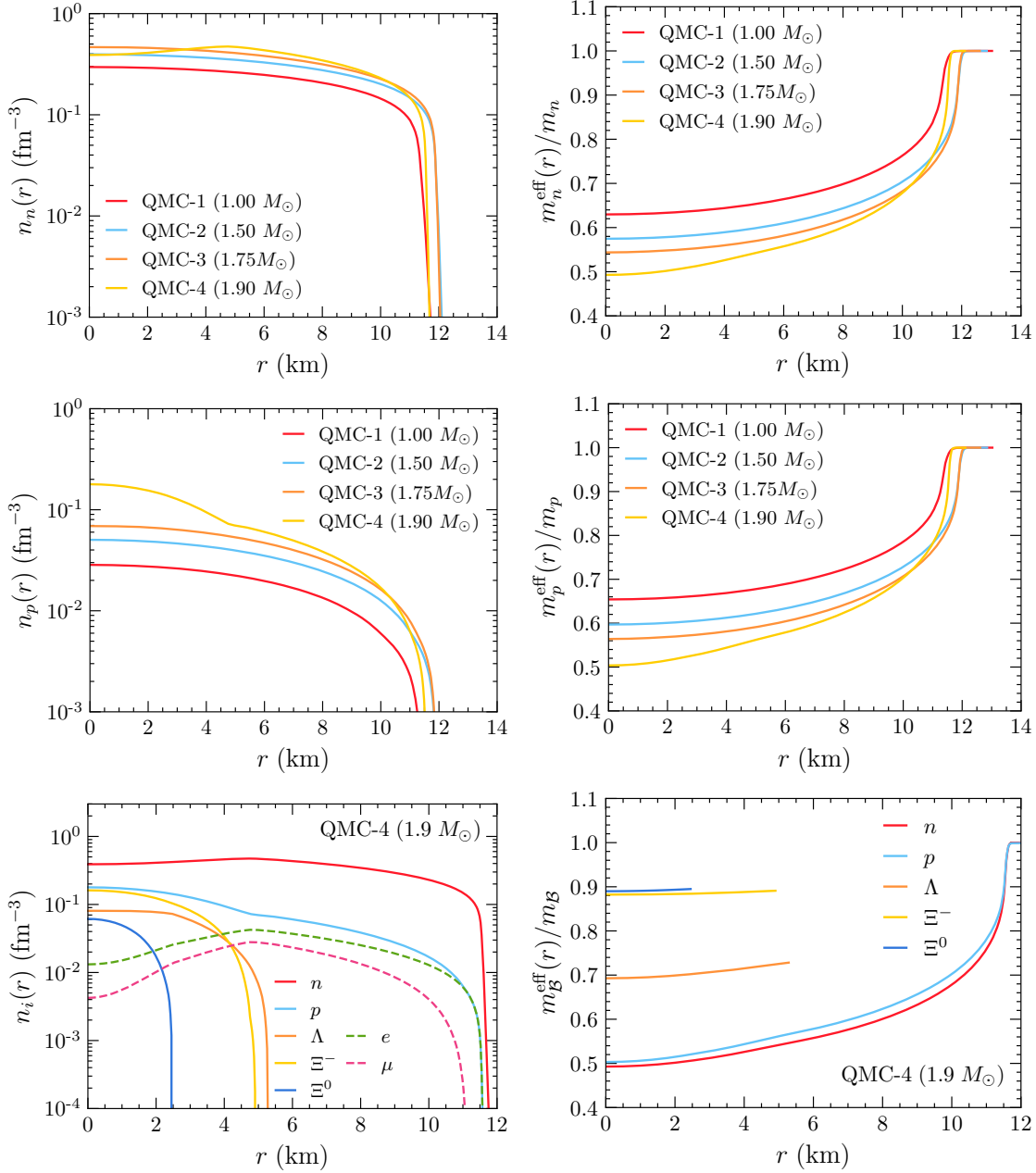


**Figure 2.5:** Number density profiles (left) and the ratio of the effective mass to the bare mass (right) for neutrons (top) and protons (middle) for benchmark configurations of the QMC EoS in Table 2.3. In the bottom panels, we show the same profiles for all species in the heaviest NS considered, QMC-4, which contains hyperonic matter.



# 3

## Dark Matter Induced Heating of Neutron Stars

We analyse the various timescales at play when determining the extent of heating dark matter can induce in neutron stars. This heating occurs in two stages. Kinetic heating requires a significant fraction of the dark matter’s kinetic energy to be deposited through scattering. Further annihilation heating requires the captures and annihilation rates to come into equilibrium. The timescales for these processes is calculated and compared to the age of the star.

### 3.1 Neutron Star Temperature from Dark Matter Heating

We now discuss the potential NS heating that can be achieved by DM scattering and annihilation. We assume a nearby NS, located in the Solar neighborhood, and thus take  $\rho_\chi = 0.4 \text{ GeV cm}^{-3}$ ,  $v_\star = 230 \text{ km s}^{-1}$  and  $v_d = 270 \text{ km s}^{-1}$  as the DM density, NS velocity, and DM dispersion velocity respectively. DM deposits energy into the NS via two mechanisms: (i) kinetic heating due to scattering with the constituents of the NS and (ii) annihilation of DM to SM particles that do not escape the star. We define the DM contribution to the temperature, measured by an observer far from the star, as  $T_\chi^\infty = \sqrt{B(R_\star)} T_\chi$ , where,  $B(r)$  is the time component of the Schwarzschild metric. Assuming black body radiation, this temperature will be given by

$$T_\chi^\infty = \left[ \frac{B^2(R_\star)}{4\pi\sigma_{\text{SB}}R_\star^2} \dot{E}_\chi \right]^{1/4}, \quad (3.1)$$

where  $\dot{E}_\chi = \dot{E}_{\chi,\text{kin}} + \dot{E}_{\chi,\text{ann}}$  is the rate of energy deposition, and we have assumed the absence of any other source of heating.

The DM kinetic energy is deposited at the rate

$$\dot{E}_{\chi,\text{kin}} \simeq m_\chi \left( \frac{1}{\sqrt{B(0)}} - 1 \right) C_{\text{geom}} f, \quad (3.2)$$

where  $C_{\text{geom}}$  is the maximum DM capture rate and  $f$  quantifies how efficiently the DM is captured,

$$f \simeq \min \left[ 1, \frac{\sum_i C_i}{C_{\text{geom}}} \right], \quad (3.3)$$

where we sum over the capture rates  $C_i$  for scattering on all baryonic species  $i$  in the star. Note that we have used  $B(0)$  in Eq. 3.2, instead of  $B(R_\star)$ , which was previously used in the literature. This is because gravitational potential energy is converted to kinetic energy as the DM falls deeper into the NS. Therefore, the total energy the DM can deposit is equal to the kinetic energy it gains when moving from infinity to the centre of the star. If this were the only source of heating, the observed temperature would be  $T_{\chi,\text{kin}}^\infty \sim 1870 \text{ K } f^{1/4}$  for the QMC-2 ( $1.5M_\odot$ ) benchmark NS. For the  $1M_\odot$  and  $1.9M_\odot$  NSs, we find  $\sim 1510 \text{ K } f^{1/4}$  and  $\sim 2240 \text{ K } f^{1/4}$ , respectively.

The annihilation of DM in the centre of the NS causes further heating. The annihilation rate  $\Gamma_{\text{ann}}$ , and hence the annihilation heating, is maximized when capture-annihilation equilibrium has been achieved. In this limit, the DM annihilation rate is given by  $\Gamma_{\text{ann}} = C/2$ . Then, the rate at which DM deposits all of its energy, both kinetic and rest-mass, can be expressed as

$$\dot{E}_{\chi,\text{kin+ann}} = \dot{E}_{\chi,\text{kin}} + 2\Gamma_{\text{ann}} m_\chi \simeq \frac{m_\chi}{\sqrt{B(0)}} C_{\text{geom}} f. \quad (3.4)$$

This rate implies a temperature of  $T_{\chi,\text{kin+ann}}^\infty \sim 2410 \text{ K } f^{1/4}$  for the  $1.5M_\odot$  NS. For the lightest NS considered ( $1M_\odot$ ) this value decreases to  $\sim 2160 \text{ K}$ , while for the heaviest NS ( $1.9M_\odot$ ), this temperature reaches  $\sim 2640 \text{ K } f^{1/4}$ . Therefore, annihilation heating contributes an additional  $\sim 400 - 650 \text{ K}$  to the NS temperature compared to kinetic heating alone, depending on the NS configuration.

## 3.2 Scattering Rate

**This section will be removed once preceding chapters are added.** The DM-baryon scattering rate is a key ingredient in both the capture and thermalisation processes. It is used in constructing the DM energy loss probability distribution

function, which, in turn, determines the probability that the DM is captured [226], and the average energy lost in each collision during the thermalisation process.

The most general expression for the DM down-scattering rate, expressed in terms of the DM-target response function  $S(q_0, q)$  [109, 226], is

$$\Gamma^-(K_\chi) = \int \frac{d^3 k'}{(2\pi)^3} \frac{1}{(2K_\chi)(2K'_\chi)(2m_i)(2m_i)} \Theta(E'_\chi - m_\chi) \Theta(q_0) S(q_0, q), \quad (3.5)$$

where

$$S(q_0, q) = 2 \int \frac{d^3 p}{(2\pi)^3} \int \frac{d^3 p'}{(2\pi)^3} \frac{m_i^2}{E_i E'_i} |\bar{M}(s, t, m_i)|^2 (2\pi)^4 \delta^4(k_\mu + p_\mu - k'_\mu - p'_\mu) \\ \times f_{\text{FD}}(E_i)(1 - f_{\text{FD}}(E'_i)) \Theta(E_i - m_i) \Theta(E'_i - m_i), \quad (3.6)$$

$k^\mu = (K_\chi, \vec{k})$  and  $k'^\mu = (K'_\chi, \vec{k'})$  are the DM initial and final momenta,  $p^\mu = (E_i, \vec{p})$  and  $p'^\mu = (E'_i, \vec{p'})$  are the target particle initial and final momenta,  $q_0 = E'_i - E_i$  is the DM energy loss,  $\vec{q} = \vec{p} - \vec{p'}$  is the three-momentum exchanged in the scattering,  $m_i$  is the mass of the target,  $|\bar{M}(s, t, m_i)|^2$  is the spin-averaged squared matrix element, and  $f_{\text{FD}}$  is the Fermi Dirac distribution. Note that the purpose of  $\Theta(q_0)$  is to select only the down-scattering interactions.

When the energy transfer is small compared to the Fermi energy, Pauli blocking strongly suppresses the scattering rate. Since the targets are in a highly degenerate Fermi plasma, we can take the target energy levels to be either full or empty in the zero temperature limit. Therefore, the interaction rate depends on the number of targets with energy  $E_i$  in the initial state, and on the number of empty final states with energy  $E_i + q_0$ , where  $q_0$  is the dark matter energy loss. As a result, the interaction rate necessarily vanishes in the limit that  $q_0 \rightarrow 0$ . More generally, Pauli blocking suppresses the differential interaction rate when  $E_i + q_0 \leq \varepsilon_{F,i}$ .

To calculate the squared matrix elements,  $|\bar{M}|^2$ , we take the DM-quark couplings to be described by the four-fermion effective field theory (EFT) operators listed in Table 1.1, where the strength of the coupling is parameterized by a cutoff scale,  $\Lambda_q$ . For each of these operators, the corresponding  $|\bar{M}|^2$  is expressed in terms of the Mandelstam variables  $s$  and  $t$ , and the DM-target mass ratio

$$\mu = \frac{m_\chi}{m_i}. \quad (3.7)$$

In the following sections, we shall derive approximations for interaction rates and timescales that depend on the form of the matrix element. We therefore define the parameter  $n$  to denote the  $t$ -dependence of the squared matrix element as

$$|\bar{M}|^2 \propto t^n, \quad (3.8)$$

with  $n = 0, 1, 2$ .

For DM interactions with baryons, the squared matrix elements contain hadronic coefficients,  $c_i^I(t)$ , which depend on the transferred momentum  $t$ . In the case of scalar and pseudoscalar interactions, these coefficients also depend on the baryon mass  $m_i$ . In general, these coefficients can be defined as a function of their values at zero momentum transfer as  $c_i^I(0)$  [227]

$$c_i^I(t) = c_i^I(0)F(t), \quad I \in \{S, P, V, A, T\}, \quad (3.9)$$

where S, P, V, A and T denote scalar, pseudoscalar, vector, axial, and tensor interactions, respectively. The coefficients  $c_i^I(0)$  are given in appendix A of ref. [215], while  $F(t)$  is the square of the dipole form-factor,

$$F(t) = \frac{1}{(1 - t/Q_0^2)^4}. \quad (3.10)$$

Note that the energy scale  $Q_0$  depends on the specific hadronic form factor. As in refs. [215, 228], we conservatively assume  $Q_0 = 1 \text{ GeV}$  for all operators and baryonic target species. The effect of the strong interactions between the baryons is incorporated in the proper calculation of the Fermi energies of the baryonic species,  $\varepsilon_{F,i}$ , and in the use of baryon effective masses for the target masses. These depend on the microphysics embedded in the EoS [215, 226].

For the collisions that result in DM capture, analytic scattering rate expressions can be obtained [226, 229] because the DM kinetic energy is always significantly higher than the NS temperature and hence the zero temperature  $T_\star \rightarrow 0$  approximation holds. During the thermalisation process, however, the DM kinetic energy and NS temperature become comparable, and so finite temperature effects become important. It is numerically intensive to calculate the interaction rate directly from Eq. 3.5 for these low temperatures, hence we keep only the lowest order thermal corrections. This amounts to a modification of the differential interaction rate, i.e. the  $q_0$  integrand of Eq. 3.5, such that

$$\frac{d}{dq_0} \Gamma^-(K_\chi, T_\star) = \frac{1}{1 - \exp(-q_0/T_\star)} \frac{d}{dq_0} \Gamma^-(K_\chi, T_\star = 0). \quad (3.11)$$

As a result, we can no longer obtain fully analytic expressions for the interaction rate. Therefore, all the results we present below have been calculated numerically.

### 3.3 Thermalisation

After becoming gravitationally bound to the NS, the DM particles continue to scatter with NS targets, losing energy in each collision until reaching thermal equilibrium at the centre of the star. We outline the calculation of the thermalisation

time in terms of the average DM energy lost in a single collision, and use first-order approximations to derive scaling relations that allow us to understand the qualitative features of our numerical results.

### 3.3.1 Average DM energy loss

The average energy a DM particle loses per collision can be calculated by weighting the DM energy loss,  $q_0$ , with the differential interaction rate. We thus obtain

$$\langle \Delta K_\chi \rangle = \frac{1}{\Gamma^-} \int_0^{q_0^{\text{MAX}}} dq_0 q_0 \frac{d\Gamma^-}{dq_0}, \quad (3.12)$$

where  $q_0^{\text{MAX}}$  is the maximum energy lost in a single scatter. Figure 3.1 shows  $q_0^{\text{MAX}}$  as a function of the DM kinetic energy,  $K_\chi = E_\chi - m_\chi$ , for DM-neutron collisions. We see that heavier DM particles lose a smaller fraction of their kinetic energy per collision than lighter DM<sup>1</sup>. Nevertheless, as  $K_\chi$  approaches the Pauli blocked region,  $K_\chi \ll m_i \varepsilon_{F,n}/m_\chi$  (dashed blue line), the maximum energy loss per collision becomes independent of the DM mass.

For the initial collision that results in the capture, Pauli blocking represents, at most, a sub-leading correction to the capture rate for DM masses above the Fermi energy of the targets. Following capture, however, the DM energy will continue to decrease as a result of subsequent scattering, eventually reaching kinetic energies where Pauli blocking is an important effect. Consequently, Pauli blocking will strongly impact the rate at which dark matter is thermalised, for a wide DM mass range that extends well above  $\varepsilon_{F,i}$ .

It is useful to define a critical DM mass, above which Pauli blocking is never in effect throughout the entire thermalisation process. We do this by analysing the regions of the interaction rate phase space that are suppressed by Pauli blocking, arriving at

$$m_\chi \gtrsim \frac{2\varepsilon_{F,i}(2m_i + \varepsilon_{F,i})}{K_\chi} = m_\chi^{\text{crit}}. \quad (3.13)$$

For neutron targets with  $\varepsilon_{F,n} = 200$  MeV, and assuming an equilibrium temperature of  $10^3$  K, i.e.  $K_\chi \gtrsim 10^3$  K, we find (neglecting the nucleon form factors)  $m_\chi^{\text{crit}} \sim 9.65 \times 10^9$  GeV.<sup>2</sup> Pauli blocking will then suppress at least some part of the thermalisation process for all DM masses below this value.

---

<sup>1</sup>In this figure, the additional suppression introduced by the momentum-dependent hadronic matrix elements is neglected.

<sup>2</sup>Note that at low energies, where  $K_\chi \ll m_\chi$ , and DM masses  $m_\chi \lesssim m_i \frac{\varepsilon_{F,i}}{K_\chi}$ , the maximum DM energy loss in a single scattering is  $q_0^{\text{MAX}} \sim K_\chi \ll \varepsilon_{F,i}$ .

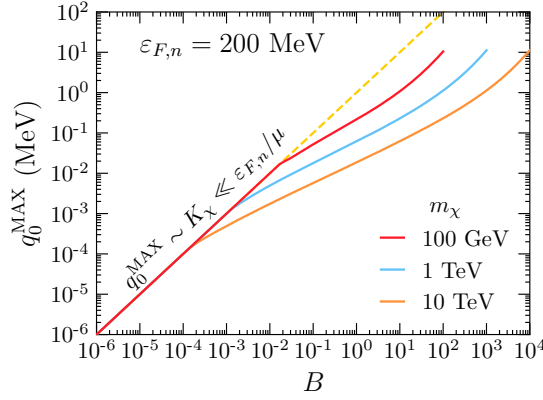


**Figure 3.1:** Maximum energy loss per collision with neutron targets, as a function of the DM kinetic energy. We have assumed  $\varepsilon_{F,n} = 200$  MeV.

In either regime, we can obtain first-order approximations for the average fraction of energy that a DM particle loses in a single collision by making use of the zero temperature approximation, a constant target mass, and nucleonic form factors at zero momentum transfer, i.e.,  $F(t) \sim 1$ . First, we consider the regime in which Pauli blocking is negligible,  $m_\chi \gtrsim m_\chi^{\text{crit}}$ . For a constant cross-section (i.e.  $|\mathcal{M}|^2 \propto t^0$ ) we find

$$\langle \Delta K_\chi^{(n=0)} \rangle \sim 2 \sqrt{\frac{\varepsilon_{F,i}}{\mu}} K_\chi^{1/2} \ll K_\chi, \quad (3.14)$$

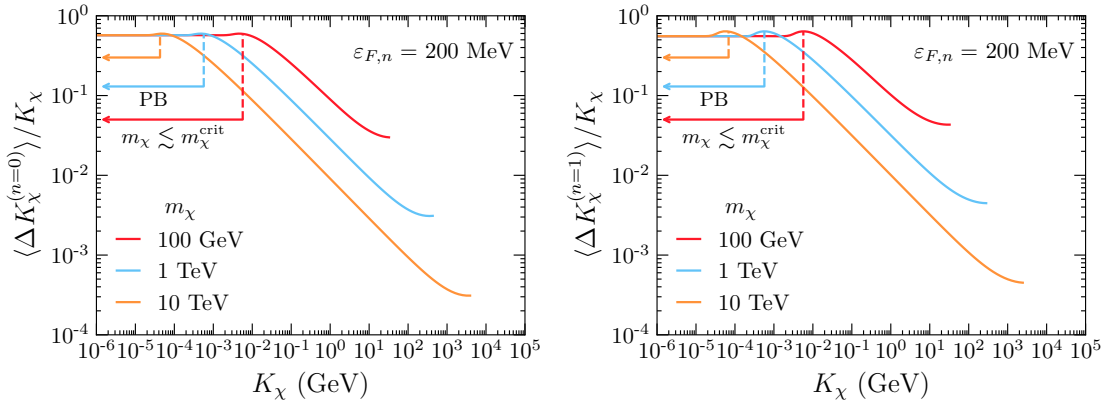
at first order in  $m_\chi^{\text{crit}}/m_\chi$ . (See appendix **ADD APPENDIX** for the corresponding approximation of the interaction rate, Eq. **IN APPENDIX**) For cross-sections proportional to  $t^1$  and  $t^2$ , the average energy losses can be obtained in the same way, starting from the relevant expressions for  $\frac{d\Gamma}{dq_0}$ .

Figure 3.2 shows the average energy loss fraction per collision. We see the  $\langle \Delta K_\chi^{(n=0)} \rangle / K_\chi \propto K_\chi^{-1/2}$  scaling of Eq. 3.14 in the  $m_\chi \gtrsim m_\chi^{\text{crit}}$  phase of the evolution, where the kinetic energy is driven down toward values where Pauli blocking eventually becomes active. The latter Pauli blocked phase is indicated by the horizontal arrows in Fig. 3.2.

Moving to the case where Pauli blocking suppresses the scattering rate,  $m_\chi \lesssim m_\chi^{\text{crit}}$ , the average energy loss per collision for the case of a constant cross-section is

$$\langle \Delta K_\chi^{(n=0)} \rangle \sim \frac{4}{7} K_\chi. \quad (3.15)$$

The average energy loss now scales linearly with  $K_\chi$  (the flat regions in Fig. 3.2) in contrast to the  $K_\chi^{1/2}$  dependence of Eq. 3.14. As the DM kinetic energy decreases,



**Figure 3.2:** Average fraction of energy loss per DM-neutron collision for constant cross-section (left) and  $d\sigma \propto t$  (right) as a function of the DM kinetic energy. Horizontal arrows indicate the Pauli blocked (PB) regime,  $m_\chi \lesssim m_\chi^{\text{crit}}$ .

the average fraction of energy transferred to the targets progressively increases until  $K_\chi$  no longer satisfies Eq. 3.13 and consequently, the interaction rate becomes Pauli blocked. As expected from Eq. 3.13, the Pauli-suppressed region starts at higher kinetic energy for lower DM masses.

For interactions with  $t$ -dependent matrix elements, the average energy loss per collision also scales linearly with  $K_\chi$  in the Pauli blocked regime. For  $|\bar{\mathcal{M}}|^2 \propto t^n$ , with  $n = 1, 2$ , we find

$$\langle \Delta K_\chi^{(n=1)} \rangle \sim \frac{5}{9} K_\chi, \quad \langle \Delta K_\chi^{(n=2)} \rangle \sim \frac{28}{55} K_\chi, \quad (3.16)$$

respectively, where we have used Eqs. [eq:intraten1](#) and [eq:intraten2](#) for the interaction rates. Note that the average energy loss fraction per collision exhibits similar behavior for all the interaction types considered, as seen by comparing the left and right panels of Fig. 3.2. This is true in both the Pauli-blocked and non-blocked regimes.

### 3.3.2 Thermalisation timescale

Once a DM particle is captured, it becomes gravitationally bound to the NS and follows an orbit that may or may not lie completely within the NS. If the orbit lies partly outside the NS, subsequent scatterings will be required for the DM particle to lose enough energy so that the complete orbit lies within the NS. This is the first stage in the thermalisation process. When estimating the amount of time needed for the DM orbit to lie completely within the star, we find that this time is always much shorter than the full time required for DM to reach thermal equilibrium with

the neutron targets. Consequently, this first step in the thermalisation process can be safely neglected. This finding is in agreement with ref. [107].

We shall also assume that up-scattering of the DM to larger kinetic energy does not play an important role<sup>3</sup>. These effects will become relevant as the DM approaches thermal equilibrium, increasing the thermalisation time. We estimate that up-scattering will, at most, increase the thermal equilibrium time by  $\mathcal{O}(10\%)$ , and thus we neglect this correction.

For DM of mass much larger than the target mass,  $m_\chi \gg m_i^{\text{eff}}$ , there is an additional stage in the thermalisation process where either Pauli blocking plays no role, or the interaction rate has a different power law relationship with the temperature than those identified in Section 3.3.1. These initial scatterings make a negligible contribution to the thermalisation time, as  $\Gamma^-$  is a sharply decreasing function of the DM kinetic energy  $K_\chi$ .

Let us denote the number of initial collisions before reaching the Pauli blocked regime as  $N_1$ , and the number of additional collisions required for complete thermalisation as  $N_2$ . For light DM,  $m_\chi \lesssim m_i^{\text{eff}}$ , Pauli blocking affects the entire thermalisation process, i.e.  $N_1 = 0$ . Let  $K_N$  be the kinetic energy after  $N$  scatterings. After  $N_1 + N_2$  collisions, the DM will reach the equilibrium temperature  $T_{\text{eq}}$ , which can be written as

$$K_{N_1+N_2} = K_{N_1} \left( 1 - \frac{\langle \Delta K_\chi \rangle}{K_\chi} \right)^{N_2} = T_{\text{eq}}, \quad (3.17)$$

where we have used the fact that the average fractional energy loss is the same in each collision. The thermalisation time can then be defined as the sum of the average time between collisions, up until the final energy transfer is equal to  $T_{\text{eq}}$  [109]

$$t_{\text{therm}} = \sum_{n=0}^{N_2} \frac{1}{\Gamma^-(K_n)} \sim \sum_{n=N_1}^{N_2} \frac{1}{\Gamma^-(K_n)}. \quad (3.18)$$

For  $m_\chi \lesssim m_\chi^{\text{crit}}$ , the fraction of energy lost in the last few scatters is still a considerable fraction of the DM kinetic energy before the collision. Furthermore, these scatterings may take a considerably long time to occur, indicating that the process is discrete. As an example, consider thermalisation to a temperature of  $10^3$  K, for a DM particle of mass  $m_\chi = 1$  TeV and constant cross-section  $\sigma_{n\chi} \sim$

---

<sup>3</sup>Up-scattering refers to collisions with negative energy transfer  $q_0 < 0$ , such that the DM particle gains energy instead of losing it. When complete thermalisation has been achieved, the rates for up-scattering and down-scattering must become equal, and hence we expect the up-scattering rates to become more significant as thermalisation is approached. If this were to be significant, our calculation below would underestimate the full thermalisation time. As we shall see, this does not impact our conclusions.

$10^{-45} \text{ cm}^2$ .<sup>4</sup> Hundreds of collisions are required to fully thermalise; the last 10 or so are spaced longer than a second apart; and the last couple are longer than 10 kyr apart.

To compute the thermalisation time, we numerically integrate Eq. 3.11 to obtain the interaction rate and the average energy lost in each collision for each of the EFT operators in Table 1.1. We find that the thermalisation time for a particular interaction type scales according to the dominant power of the Mandelstam variable  $t$  in the corresponding matrix element; see the last column of Table 1.1. Thus, to understand how the thermalisation times scale, it is enough to consider differential cross-sections that are proportional to a given power of  $t$ , i.e.  $d\sigma \propto t^n$ , with  $n = 0, 1, 2$ . Below, we present results for operators that depend only on  $t$  (D1-4 in Table 1.1), and not on the centre of mass energy,  $s$ . In Appendix **Add s dep appendix**, we outline the procedure used to obtain analytic expressions for those operators with an explicit dependence on  $s$  (operators D5-10).

In Figure 3.3, we show the full numerical results for the thermalisation time as a function of the DM mass for different equilibrium temperatures. It is clear that the power law scaling of the thermalisation time with DM mass depends on whether  $m_\chi$  is larger or smaller than the nucleon mass. To understand these results, we make use of the analytic approximations for the average DM energy loss derived in Section 3.3.1 and valid in the zero temperature limit.

We begin by studying the Pauli blocked regime,  $m_\chi \lesssim m_\chi^{\text{crit}}$ . In this case, the majority of the thermalisation time is dictated by the final few scatters, for which the form factors are close to their value at zero momentum transfer. These last collisions occur close to the NS centre, so we can take the target mass as constant and equal to the value at the centre of the star,  $m_i^{\text{eff}}(0)$ . For the case of a constant DM-neutron cross-section,  $d\sigma \propto t^0$ , the thermalisation time can thus be obtained by using Eqs. [eq:intraten0](#), 3.17 and 3.15 in Eq. 3.18. This leads to

$$t_{\text{therm}}^{(n=0)} \sim \frac{147}{16} \frac{\pi^2 m_\chi}{(m_i^{\text{eff}}(0) + m_\chi)^2} \frac{1}{\sigma_{i\chi}^{n=0}} \frac{1}{T_{\text{eq}}^2}, \quad (3.19)$$

where  $\sigma_{i\chi}^{n=0}$  is the DM-baryon cross-section. The scaling of this expression with  $T_{\text{eq}}$ , DM mass, and DM-target cross-sections agrees with ref. [109]. Numerically we obtain

$$t_{\text{therm}}^{(n=0)} \sim \begin{cases} 4.4 \times 10^6 \text{ yrs} \left( \frac{m_\chi}{10 \text{ MeV}} \right) \left( \frac{10^{-45} \text{ cm}^2}{\sigma_{i\chi}^{n=0}} \right) \left( \frac{10^3 K}{T_{\text{eq}}} \right)^2, & m_\chi \ll m_i^{\text{eff}}(0) \\ 9.7 \times 10^6 \text{ yrs} \left( \frac{10 \text{ GeV}}{m_\chi} \right) \left( \frac{10^{-45} \text{ cm}^2}{\sigma_{i\chi}^{n=0}} \right) \left( \frac{10^3 K}{T_{\text{eq}}} \right)^2, & m_\chi \gg m_i^{\text{eff}}(0) \end{cases} \quad (3.20)$$

where we have set  $m_i^{\text{eff}}(0) = 0.5 m_n$ . The  $m_\chi$  dependence of these expressions

---

<sup>4</sup>For a wide DM mass range (GeV–TeV), this value is comparable to the cross-section that results in maximal capture, and hence we will use this cross-section as a reference value in some of the estimates that follow.

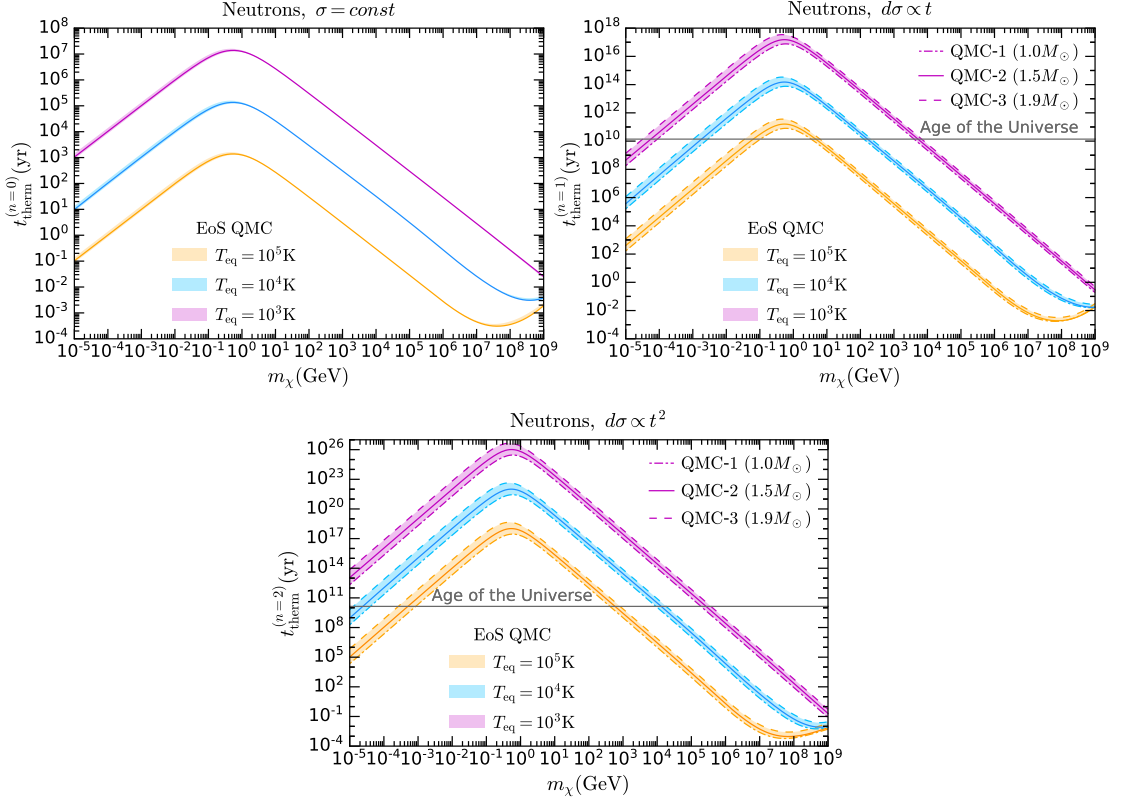


**Figure 3.3:** thermalisation time as a function of the DM mass for constant cross-section (top left),  $d\sigma \propto t$  (top right) and  $d\sigma \propto t^2$  (bottom). We have used the NS benchmark models in Table 2.3 and a reference cross-section of  $\sigma_{n\chi} = 10^{-45} \text{ cm}^2$  close to the NS surface. Shaded regions indicate the variation with the choice of EoS: QMC-1 (dot-dashed), QMC-2 (solid), and QMC-3 (dashed).

explains the features observed in the top left panel of Fig. 3.3. For  $m_\chi \ll m_i^{\text{eff}}(0)$ , the thermalisation time scales with the DM mass as the number of scatterings needed for thermalisation increases. Conversely, for  $m_\chi \gg m_i^{\text{eff}}(0)$ ,  $t_{\text{therm}}^{(n=0)}$  is inversely proportional to  $m_\chi$  due to the reduced Pauli blocking, explaining the change of slope around the value of the neutron effective mass in the NS centre.

We repeat the same analysis for cross-section proportional to higher powers of  $t$ , i.e.,  $d\sigma \propto t^n$  with  $n = 1, 2$ . Using Eqs. eq:intraten1, eq:intraten2 and 3.16, we find

$$t_{\text{therm}}^{(n=1)} \sim 14 \frac{\pi^2 m_\chi^2 (m_i^{\text{eff}}(0))^2}{(m_i^{\text{eff}}(0) + m_\chi)^2 ((m_i^{\text{eff}}(0))^2 + m_\chi^2)} \frac{1}{\sigma_{i\chi}^{n=1}} \frac{1}{T_{\text{eq}}^3} \frac{1 - B(R_\star)}{B(R_\star)}, \quad (3.21)$$

$$t_{\text{therm}}^{(n=2)} \sim 17 \frac{\pi^2 m_\chi^3 (m_i^{\text{eff}}(0))^4}{(m_i^{\text{eff}}(0) + m_\chi)^2 ((m_i^{\text{eff}}(0))^2 + m_\chi^2)^2} \frac{1}{\sigma_{i\chi}^{n=2}} \frac{1}{T_{\text{eq}}^4} \left[ \frac{1 - B(R_\star)}{B(R_\star)} \right]^2, \quad (3.22)$$

where the factors involving  $B(R_\star)$  arise from fixing the cross-section to its value at the surface; see Appendix sec:pauliblocking for details.

To gain insight into the order of magnitude of these thermalisation times, we set  $B(R_\star) = 0.5$  and  $m_i^{\text{eff}}(0) = 0.5 m_n$ , yielding

$$t_{\text{therm}}^{(n=1)} \sim \begin{cases} 2.5 \times 10^{14} \text{ yrs} \left( \frac{m_\chi}{10 \text{ MeV}} \right)^2 \left( \frac{10^{-45} \text{ cm}^2}{\sigma_{i\chi}^{n=1}} \right) \left( \frac{10^3 K}{T_{\text{eq}}} \right)^3, & m_\chi \ll m_i^{\text{eff}}(0) \\ 3.9 \times 10^{15} \text{ yrs} \left( \frac{10 \text{ GeV}}{m_\chi} \right)^2 \left( \frac{10^{-45} \text{ cm}^2}{\sigma_{i\chi}^{n=1}} \right) \left( \frac{10^3 K}{T_{\text{eq}}} \right)^3, & m_\chi \gg m_i^{\text{eff}}(0) \end{cases} \quad (3.23)$$

$$t_{\text{therm}}^{(n=2)} \sim \begin{cases} 1.1 \times 10^{23} \text{ yrs} \left( \frac{m_\chi}{10 \text{ MeV}} \right)^3 \left( \frac{10^{-45} \text{ cm}^2}{\sigma_{i\chi}^{n=2}} \right) \left( \frac{10^3 K}{T_{\text{eq}}} \right)^4, & m_\chi \ll m_i^{\text{eff}}(0) \\ 1.2 \times 10^{24} \text{ yrs} \left( \frac{10 \text{ GeV}}{m_\chi} \right)^3 \left( \frac{10^{-45} \text{ cm}^2}{\sigma_{i\chi}^{n=2}} \right) \left( \frac{10^3 K}{T_{\text{eq}}} \right)^4, & m_\chi \gg m_i^{\text{eff}}(0). \end{cases} \quad (3.24)$$

As anticipated, we see that the momentum-suppressed cross-sections translate into significantly longer thermalisation times than for the case of a constant (un-suppressed) cross-section. These expressions also allow us to understand the dependence of  $t_{\text{therm}}$  on the DM mass. For  $d\sigma \propto t^n$ , the thermalisation time scales as  $m_\chi^{n+1}$  for  $m_\chi \ll m_i^{\text{eff}}(0)$ , and as the inverse of this quantity for  $m_\chi \gg m_i^{\text{eff}}(0)$ .

The choice of EoS has a small but non-negligible impact on the thermalisation time, as indicated by the widths of the shaded regions in Fig. 3.3. For a constant cross-section, we observe almost no variation in  $t_{\text{therm}}$  with the NS configuration, except for the  $m_\chi \lesssim m_n$  region. This is due to the dependence of  $m_n^{\text{eff}}(0)$  on the NS model; see Table 2.3 and Eq. 3.19. For cross-sections  $d\sigma \propto t^n$ , with  $n = 1, 2$ , the dependence on  $B(R_\star)$  in Eqs. 3.21 and 3.22 adds an extra dependence on the choice of NS model. For these momentum-suppressed interactions, DM requires more time to reach an equilibrium temperature in heavier NSs. This is due to the

combination of two effects: the effective mass of the targets in the centre of the NS is smaller in more massive NS configurations, while  $B(R_\star)$  increases. Nonetheless, the dependence on NS configuration remains relatively mild.

We now turn to the  $m_\chi \gtrsim m_\chi^{\text{crit}}$  regime, which is observed only for temperatures above  $10^4$  K in Fig. 3.3. This regime change is indicated by the change of slope that occurs at large DM masses, clearly evident for  $T_{\text{eq}} = 10^5$  K (orange) at a DM of mass  $m_\chi \gtrsim 5 \times 10^7$  GeV. In this regime, the energy lost in each collision is a tiny fraction of the initial DM kinetic energy, and the time between scatterings is of order a fraction of a second. This indicates that a continuous approximation becomes more appropriate than a discrete sum to estimate  $t_{\text{therm}}$ . In this case, the momentum-dependent part of the form factor,  $F(t)$ , will be relevant only at the beginning of the thermalisation process and become less and less relevant as the average momentum transfer decreases in each subsequent scatter.<sup>5</sup> It is these low momentum-transfer collisions that dominate the thermalisation time. For a constant cross-section ( $n = 0$ ), in the zero temperature approximation, we obtain (see Appendix sec:thermsuperheavy for details)

$$t_{\text{therm}}^{(n=0)} \sim \frac{9\pi^2 m_\chi}{8(m_i^{\text{eff}}(0))^2 \varepsilon_{F,i}^2 \sigma_{i\chi}^{n=0}} \log \left[ \frac{m_\chi}{T_{\text{eq}}} \left( \frac{1}{\sqrt{B(R_\star)}} - 1 \right) \right]. \quad (3.25)$$

In this super heavy DM mass regime, we see that the thermalisation time is an increasing function of  $m_\chi$ .

It is worth remarking that for a constant DM-neutron cross-section (top left panel) thermalisation will always occur within the age of the Universe. However, this is not true for momentum-suppressed cross-sections, for a range of DM masses. Specifically, for  $T_{\text{eq}} = 10^3$  K and the assumed reference cross-section, DM of mass  $m_\chi \lesssim 10$  TeV ( $m_\chi \lesssim 1$  PeV) will not have enough time to thermalise for  $d\sigma \propto t$  ( $d\sigma \propto t^2$ ). Importantly, however, we shall see below that even when full thermalisation takes longer than the age of the Universe, the majority of the kinetic energy is deposited on a much shorter timescale.

Finally, we must incorporate the fact that DM will scatter with various baryonic species in the NS rather than just the neutrons. To do this, the thermalisation times from scattering off each species are combined appropriately based on their abundances. Specifically, we sum the inverse single-species thermalisation times, weighted by their relative abundance at the centre of the NS, such that

$$\frac{1}{t_{\text{therm, tot}}} = \sum_i \frac{Y_i(0)}{t_{\text{therm}, i}}, \quad (3.26)$$

where  $Y_i(0)$  is the abundance of the species in the centre of the NS, and the sum runs over all possible baryons. For the case of the heaviest NS we consider,  $1.9 M_\odot$ ,

---

<sup>5</sup>We have numerically verified that the  $t$ -dependent form factors do not alter the results in any significant manner.

this includes the  $\Lambda^0$ ,  $\Xi^0$  and  $\Xi^-$  hyperons. The resulting thermalisation time then lies between the fastest and slowest single-species times, as is expected.

## 3.4 Capture-Annihilation Equilibrium

The captured DM will accumulate in the centre of the NS, where it will begin to annihilate. The annihilation rate will grow until sufficient time has elapsed for the capture and annihilation processes to reach equilibrium. In this limit, the total amount of DM in the NS is maximised and will remain constant. Once this occurs, annihilation efficiently deposits the DM mass-energy into the star.

Let us begin by assuming that the dark matter has fully thermalised. After reviewing the standard capture-annihilation equilibrium calculation, we will relax this assumption to consider the more general case of partially thermalised dark matter and derive new expressions that hold in that scenario. Importantly, we shall see that capture-annihilation equilibrium, and hence efficient annihilation can occur without full thermalisation.

### 3.4.1 Capture-annihilation equilibrium of thermalised dark matter

The thermalised DM will collect within an isothermal sphere at the centre of the NS where it will begin to annihilate. The efficiency of the annihilation will depend on the volume of this sphere, which is expected to be very small for the DM masses we consider. Very close to the centre of the NS, the density does not vary significantly and can be taken to be constant. Then, working in the weak field approximation such that  $B(r) \sim 1 + 2\Phi(r)$ , we can obtain the gravitational potential inside the NS,

$$\Phi(r) = - \int_r^\infty \frac{GM_\star(r')}{r'^2} dr' \approx \frac{2}{3}\pi G\rho_c r^2, \quad (3.27)$$

where  $\rho_c$  is the central density of the NS. The number density of DM particles that have thermalised to a temperature  $T_{\text{eq}}$  as a function of radius will then be given by a Maxwell-Boltzmann distribution

$$n_\chi(r) \simeq n_0 \exp \left[ -\frac{m_\chi \Phi(r)}{T_{\text{eq}}} \right] = \frac{N_\chi}{\pi^{3/2} r_{\text{iso}}^3} \exp \left( -\frac{r^2}{r_{\text{iso}}^2} \right), \quad (3.28)$$

where  $N_\chi$  is the total number of DM particles within the isothermal sphere, and  $r_{\text{iso}}$  is the radius of the DM isothermal sphere. Applying the viral theorem leads to

the following expression for  $r_{\text{iso}}$ ,

$$\begin{aligned} r_{\text{iso}} &= \sqrt{\frac{3T_{\text{eq}}}{2\pi G m_\chi \rho_c}} \\ &\approx 0.26 \text{ m} \left[ \left( \frac{T_{\text{eq}}}{10^3 \text{ K}} \right) \left( \frac{1 \text{ GeV}}{m_\chi} \right) \left( \frac{8 \times 10^{14} \text{ g cm}^{-3}}{\rho_c} \right) \right]^{1/2}. \end{aligned} \quad (3.29)$$

The total number of DM particles enclosed in this sphere is then

$$N_\chi \simeq 4\pi \int dr r^2 n_\chi(r), \quad (3.30)$$

and the velocity distribution of the thermalised DM is given by

$$f_{\text{MB}}(v_\chi) = 4\pi \left( \frac{m_\chi}{4\pi T_{\text{eq}}} \right)^{3/2} v_\chi^2 \exp \left[ -\frac{m_\chi v_\chi^2}{4T_{\text{eq}}} \right]. \quad (3.31)$$

In the absence of evaporation, which can safely be neglected for  $m_\chi \gtrsim 1.17 \times 10^{-8} \text{ GeV}$  for a Gyr old NS with core temperature  $\sim 10^3 \text{ K}$  [229], the time evolution of the total number of DM particles present inside the NS is governed by

$$\frac{dN_\chi}{dt} = C - AN_\chi^2. \quad (3.32)$$

Here  $C$  is the capture rate and  $A$  is related to the DM annihilation rate,  $\Gamma_{\text{ann}}$ , through

$$\Gamma_{\text{ann}} = \frac{1}{2}AN_\chi^2, \quad (3.33)$$

where

$$A = \frac{\langle \sigma_{\text{ann}} v_\chi \rangle}{N_\chi^2} \int n_\chi^2(r) d^3r \simeq \frac{\langle \sigma_{\text{ann}} v_\chi \rangle}{(2\pi)^{3/2} r_{\text{iso}}^3}, \quad (3.34)$$

and  $\langle \sigma_{\text{ann}} v_\chi \rangle$  is the thermally averaged DM annihilation cross-section. These are given in Table 3.1 for the EFT interactions we consider, where  $\langle v_\chi^2 \rangle = v_{\text{th}}^2 = 6T_{\text{eq}}/m_\chi$ .

We note that the cross-sections shown in Table 3.1 are quark-level expressions. For most of the mass range of interest, these provide excellent approximations to the hadron-level annihilation cross-sections, provided we impose a lower bound on the DM mass for which an annihilation channel is open, taken to be the pion mass. See Appendix [sec:quarkhadron](#) for details.

Name	Operator	$\langle \sigma_{ann} v_\chi \rangle$
D1	$\bar{\chi}\chi \bar{q}q$	$\frac{3m_\chi^2}{8\pi\Lambda^4} \sum_q y_q^2 \left(1 - \frac{m_q^2}{m_\chi^2}\right)^{3/2} v_{\text{th}}^2$
D2	$\bar{\chi}\gamma^5\chi \bar{q}q$	$\frac{3m_\chi^2}{2\pi\Lambda^4} \sum_q y_q^2 \sqrt{1 - \frac{m_q^2}{m_\chi^2}} \left[ \left(1 - \frac{m_q^2}{m_\chi^2}\right) + \frac{3}{8} \frac{m_q^2}{m_\chi^2} v_{\text{th}}^2 \right]$
D3	$\bar{\chi}\chi \bar{q}\gamma^5 q$	$\frac{3m_\chi^2}{8\pi\Lambda^4} \sum_q y_q^2 \sqrt{1 - \frac{m_q^2}{m_\chi^2}} v_{\text{th}}^2$
D4	$\bar{\chi}\gamma^5\chi \bar{q}\gamma^5 q$	$\frac{3m_\chi^2}{2\pi\Lambda^4} \sum_q y_q^2 \sqrt{1 - \frac{m_q^2}{m_\chi^2}} \left[ 1 + \frac{m_q^2}{8(m_\chi^2 - m_q^2)} v_{\text{th}}^2 \right]$
D5	$\bar{\chi}\gamma_\mu\chi \bar{q}\gamma^\mu q$	$\frac{3m_\chi^2}{2\pi\Lambda^4} \sum_q \sqrt{1 - \frac{m_q^2}{m_\chi^2}} \left[ \left(2 + \frac{m_q^2}{m_\chi^2}\right) + \left(\frac{-4m_\chi^4 + 2m_q^2 m_\chi^2 + 11m_q^4}{24m_\chi^2(m_\chi^2 - m_q^2)}\right) v_{\text{th}}^2 \right]$
D6	$\bar{\chi}\gamma_\mu\gamma^5\chi \bar{q}\gamma^\mu q$	$\frac{m_\chi^2}{4\pi\Lambda^4} \sum_q \sqrt{1 - \frac{m_q^2}{m_\chi^2}} \left[ 2 + \frac{m_q^2}{m_\chi^2} \right] v_{\text{th}}^2$
D7	$\bar{\chi}\gamma_\mu\chi \bar{q}\gamma^\mu\gamma^5 q$	$\frac{3m_\chi^2}{\pi\Lambda^4} \sum_q \sqrt{1 - \frac{m_q^2}{m_\chi^2}} \left[ \left(1 - \frac{m_q^2}{m_\chi^2}\right) - \frac{1}{24} \left(2 - 11 \frac{m_q^2}{m_\chi^2}\right) v_{\text{th}}^2 \right]$
D8	$\bar{\chi}\gamma_\mu\gamma^5\chi \bar{q}\gamma^\mu\gamma^5 q$	$\frac{3m_\chi^2}{2\pi\Lambda^4} \sum_q \sqrt{1 - \frac{m_q^2}{m_\chi^2}} \left[ \frac{m_q^2}{m_\chi^2} + \left(\frac{8m_\chi^4 - 28m_\chi^2 m_q^2 + 23m_q^4}{24m_\chi^2(m_\chi^2 - m_q^2)}\right) v_{\text{th}}^2 \right]$
D9	$\bar{\chi}\sigma_{\mu\nu}\chi \bar{q}\sigma^{\mu\nu} q$	$\frac{6m_\chi^2}{\pi\Lambda^4} \sum_q \sqrt{1 - \frac{m_q^2}{m_\chi^2}} \left[ \left(1 + 2 \frac{m_q^2}{m_\chi^2}\right) - \left(\frac{2m_\chi^4 + 17m_q^2 m_\chi^2 - 28m_q^4}{24m_\chi^2(m_\chi^2 - m_q^2)}\right) v_{\text{th}}^2 \right]$
D10	$\bar{\chi}\sigma_{\mu\nu}\gamma^5\chi \bar{q}\sigma^{\mu\nu} q$	$\frac{6m_\chi^2}{\pi\Lambda^4} \sum_q \sqrt{1 - \frac{m_q^2}{m_\chi^2}} \left[ \left(1 - \frac{m_q^2}{m_\chi^2}\right) - \frac{1}{24} \left(2 - 17 \frac{m_q^2}{m_\chi^2}\right) v_{\text{th}}^2 \right]$

**Table 3.1:** Thermally averaged annihilation cross-sections  $\langle \sigma_{\text{ann}} v_\chi \rangle$  for the dimension 6 EFT operators, expanded to second order in  $v_\chi$ . The  $y_q$  factors are the quark Yukawa couplings [230].

The solution to Eq. 3.32 in terms of the capture and annihilation rates is

$$N_\chi(t) = \sqrt{\frac{C}{A}} \tanh \left( \sqrt{CA} t \right). \quad (3.35)$$

Ultimately, we are interested in the behavior of Eq. 3.35 at late stages in the NS evolution, i.e., for  $t \rightarrow t_*$ , where  $t_*$  is the age of the NS, which we take to be  $\sim 1$  Gyr. In this limit, the hydrostatic NS structure, and hence the capture rate, are not expected to change with time. Of particular interest is whether or not an equilibrium is reached between the capture and annihilation rates. Such a state is reached for timescales greater than

$$t_{\text{eq}} = \frac{1}{\sqrt{CA}}. \quad (3.36)$$

For earlier times,  $t < t_{\text{eq}}$ , one can neglect the loss of DM particles due to annihilation, leaving  $N_\chi \sim Ct$ .

### 3.4.2 Capture-annihilation equilibrium of partially thermalised dark matter

The standard calculation of the annihilation rate, using Eq. 3.34, assumes that the DM has thermalised, i.e.,  $t > t_{\text{therm}}$ . If thermalisation has not been achieved by a time  $t \sim t_* < t_{\text{therm}}$ , the DM kinetic energy distribution will peak around the lowest temperature that DM has had enough time to reach. This is given by

$$K_\chi \sim T_{\text{eq}} \left( \frac{t_{\text{therm}} + t_*}{t_*} \right)^{\frac{1}{2+n}}, \quad (3.37)$$

where  $n$  is the exponent of the dominant  $t^n$  term in the differential cross-section,  $d\sigma \propto t^n$ , as given in the last column of Table 1.1. See Appendix sec:minTempDerivation for details. We can then find the radius of the DM distribution (which is no longer isothermal) and the  $\langle \sigma_{\text{ann}} v_\chi \rangle$  corresponding to the peak of the energy distribution  $K_\chi$ . We obtain  $A$  via the replacement

$$A \rightarrow A \left( \frac{T_{\text{eq}}}{K_\chi} \right)^\alpha = A \left( \frac{t_*}{t_{\text{therm}} + t_*} \right)^{\frac{\alpha}{2+n}}, \quad (3.38)$$

where  $\alpha = 3/2$  for  $s$ -wave annihilation, and  $\alpha = 1/2$  for  $p$ -wave. Making this replacement in Eq. 3.36 leads to a capture-annihilation equilibrium time of

$$t_{\text{eq}} = \frac{1}{\sqrt{CA}} \left( \frac{t_{\text{therm}} + t_*}{t_*} \right)^{\frac{\alpha}{2(2+n)}}. \quad (3.39)$$

No previous estimate of the capture-annihilation equilibrium time has considered the case of partially thermalised DM. If thermalisation has not been achieved, the additional factor in Eq. 3.39, compared to Eq. 3.36, increases the equilibrium time. (Or, equivalently, increases the cross-sections required to reach equilibrium within a specified time.) However, it is critical to realize that  $t_{\text{eq}}$  can be shorter than  $t_{\text{therm}}$ . In fact, annihilation can occur efficiently even if complete thermalisation never occurs. In this scenario, we must use Eq. 3.39.

Assuming the DM is captured at the geometric limit, we arrive at the following result for our benchmark NS QMC-2

$$\begin{aligned} t_{\text{eq}} \sim & 4 \times 10^{-6} \text{ yr} \left( \frac{100 \text{ GeV}}{m_\chi} \right)^{\frac{1}{4}} \left( \frac{10^{-26} \text{ cm}^3 \text{ s}^{-1}}{\langle \sigma_{\text{ann}} v_\chi \rangle} \right)^{\frac{1}{2}} \left( \frac{1 \text{ GeV cm}^{-3}}{\rho_\chi} \right)^{\frac{1}{2}} \left( \frac{T_{\text{eq}}}{10^3 \text{ K}} \right)^{\frac{3}{4}} \\ & \times \left( \frac{t_{\text{therm}} + t_*}{t_*} \right)^{\frac{\alpha}{2(2+n)}}. \end{aligned} \quad (3.40)$$

Comparing this expression with the thermalisation times in the previous section, we anticipate that  $t_{\text{eq}}$  will typically be shorter than  $t_{\text{therm}}$ , often by many orders of magnitude.

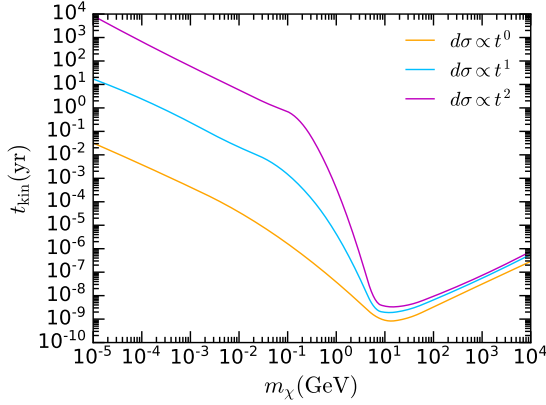


**Figure 3.4:** Timescale on which the DM deposits 99% of its initial kinetic energy in the NS. We have assumed an NS with configuration QMC-2, and a DM-neutron scattering cross-section of  $\sigma_{n\chi} = 10^{-45} \text{ cm}^2$  at the surface of the star.

## 3.5 Neutron Star Heating Timescales

### 3.5.1 Kinetic heating timescale

It has commonly been assumed that the DM kinetic energy deposition occurs instantaneously. However, it is not immediately obvious that this is true. In particular, for scattering interactions suppressed by powers of the momentum transfer,  $t$ , full thermalisation can take longer than the age of the Universe. We must therefore determine whether a *significant fraction* of the initial kinetic energy can be deposited on a shorter timescale.

To quantify the timescale on which kinetic heating takes place, we define  $t_{\text{kin}}$  to be the time required for a DM particle to lose 99% of its maximum kinetic energy,  $K_\chi = m_\chi(1/\sqrt{B(0)} - 1)$ . This time is calculated in the same way as the thermalisation time, while also keeping track of the time the DM spends outside the star along its orbit, i.e., the initial stage of the thermalisation process that was neglected in Section 3.3.2. For simplicity, the DM particle orbits are taken to be linear, passing through the centre of the star, with the radial extent calculated using the geodesic equations. We expect an  $\mathcal{O}(1)$  correction to our results when considering circular orbits. Additionally, we randomize the radial position in the NS where the DM interacts with a target.

Figure 3.4 shows the time required for kinetic heating to be achieved, assuming DM-neutron interactions of the form  $d\sigma \propto t^n$ , with cross-sections normalized to  $\sigma_{n\chi} = 10^{-45} \text{ cm}^2$  at the surface of the star. As the location of each interaction is randomized, these results are obtained by averaging over several simulations for

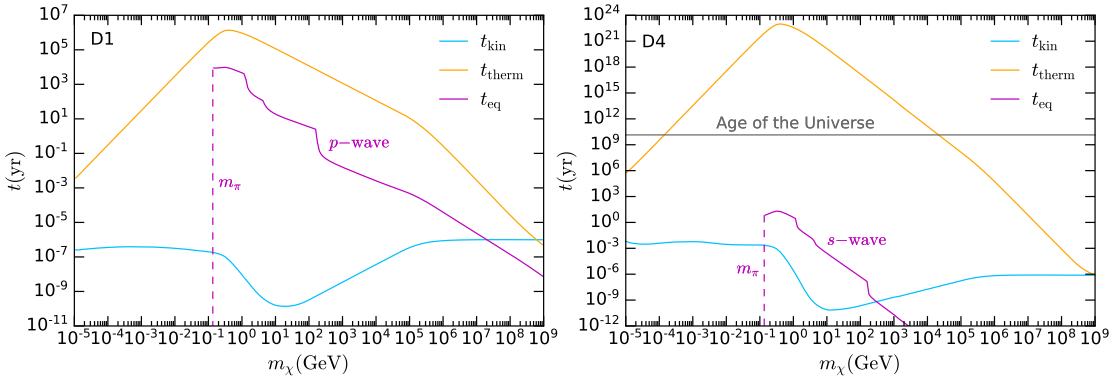


**Figure 3.5:** Timescales for kinetic heating (blue), thermalisation (orange), and capture-annihilation equilibrium (magenta), for operators D1 (left) and D4 (right). The operator D1 has an unsuppressed scattering cross-section and a  $p$ -wave suppressed annihilation cross-section, while D4 has a  $q_{\text{tr}}^4$  suppressed scattering cross-section and an unsuppressed ( $s$ -wave) annihilation cross-section. The interaction strength has been chosen to give maximal capture. (Specifically, we used  $\Lambda_q$  values corresponding to a capture cross-section at the geometric limit, assuming scattering with the neutron targets in the QMC-2 NS.)

each DM mass. For light DM,  $t_{\text{kin}}$  decreases with increasing DM mass, due to the decreased effects of Pauli blocking, with the change of slope at  $m_\chi \sim 0.1$  GeV indicating the point where Pauli blocking affects only a fraction of the total process. For masses  $\gtrsim 10$  GeV, Pauli blocking is not relevant to this part of the thermalisation process, and hence the  $t_{\text{kin}}$  monotonically increases with the DM mass, as was seen in the thermalisation of super-heavy DM.

Fig. 3.4 illustrates two key facts. First,  $t_{\text{kin}}$  differs by orders of magnitude for the different cross-section types,  $d\sigma \propto t^n$ , with larger values of  $t_{\text{kin}}$  for the most highly momentum-suppressed interactions, as expected. Second, and importantly, the kinetic heating occurs relatively quickly for all interaction types, on timescales much shorter than a typical NS age. Indeed, for the case of a constant cross-section,  $t_{\text{kin}}$  is much shorter than a year.

### 3.5.2 Annihilation heating timescale

Figure 3.5 shows all relevant timescales for DM-induced heating of old neutron stars. These timescales have been calculated considering DM scattering off the neutron targets in the benchmark NS QMC-2, for the case of maximal capture,  $f = 1$  (i.e., we have set the EFT parameter  $\Lambda_q$  as required to achieve capture at the geometric limit). We show these results for two indicative operators: The

scalar-scalar interaction D1 (left), which has a  $p$ -wave suppressed annihilation cross-section, and the pseudoscalar-pseudoscalar operator D4 (right), which has an  $s$ -wave annihilation cross-section.

As anticipated, capture-annihilation equilibrium takes longer to achieve for the velocity-suppressed  $p$ -wave annihilation cross-section than for the  $s$ -wave. Nonetheless, equilibrium (and hence maximal annihilation heating) is reached relatively quickly in both cases, on timescales of  $10^4$  years for the scalar interaction, and even quicker for the pseudoscalar, well within the age of a typical NS.

For both interaction types, the kinetic and annihilation heating contributions are both realized on timescales much shorter than that required for full thermalisation. If the scattering cross-section is momentum suppressed (as with the  $d\sigma \propto t^2 = q_{\text{tr}}^4$  dependence for D4), the thermalisation time is increased; if the annihilation cross-section is velocity suppressed (as with the  $p$ -wave annihilation cross-section for D1) the capture-annihilation equilibrium time is increased.

Finally, note that there are parameters for which the annihilation timescale  $t_{\text{eq}}$  is shorter than the kinetic heating timescale  $t_{\text{kin}}$ . In this case, the annihilation process deposits the DM mass energy and any remaining kinetic energy, which is carried by the annihilation products. Therefore, the minimum time required for DM to deposit *all* of its energy, both kinetic and rest-mass, is  $t_{\text{eq}}$ .

### 3.5.3 Neutron star heating sensitivity for various interaction types

We now examine the regions of parameter space where maximal heating can be achieved, for DM-hadron interactions described by the four-fermion operators of Table 1.1. As the extent of DM-induced heating depends on how efficiently the DM is captured, it is clear that maximal heating corresponds to the case of  $f = 1$  in Eqs. 3.2 and 3.4, i.e., when the dark matter scattering cross-section is at or above the geometric limit.

In Figure 3.6, we show the parameters for which the DM deposits its entire kinetic and rest mass energy (yellow region) or only its full kinetic energy (light blue region). Above these shaded regions, the value of  $\Lambda_q$  is too large (and hence the scattering cross-section is too small) for maximal capture. The overall shape of the shaded regions is dictated by the behaviour of the capture rate. For sub-GeV DM, Pauli blocking suppresses the capture rate, and so smaller  $\Lambda_q$  values are required to reach the geometric limit. At large DM mass,  $\gtrsim 10^5$  GeV, the capture rate is suppressed because a single collision does not transfer enough energy to result in capture.

We see from the  $t_{\text{eq}}$  contours (magenta) that capture-annihilation equilibrium, and hence full annihilation heating, is achieved on a timescale much shorter than the

NS lifetime, which we take to be  $t_* \sim 1$  Gyr. We do not show the contours for the kinetic heating timescale,  $t_{\text{kin}}$ , as this is significantly shorter than the age of the star. Moreover, for masses where DM annihilation to hadrons is possible,  $m_\chi > m_\pi$ , it is not necessary for kinetic heating to occur before capture-annihilation equilibrium is established, as the total kinetic plus mass energy will be deposited when the DM annihilates. For completeness, we include the contours of the thermalisation time (grey). We stress again that the DM does not need to fully thermalise to achieve maximal heating.

To highlight how the sensitivity varies for different interaction types, we show results for operators D1, D4 and D5 in Figure 3.6, with the remaining operators presented in Figure [fig:NSheating2](#). These operators were chosen because they allow us to compare interactions with and without momentum or velocity-suppressed scattering or annihilation cross-sections. Specifically:

- D1 (scalar): unsuppressed scattering cross-section;  $p$ -wave suppressed annihilation.
- D4 (pseudoscalar):  $q_{\text{tr}}^4$  suppressed scattering cross-section; unsuppressed  $s$ -wave annihilation.
- D5 (vector): unsuppressed scattering and annihilation cross-sections.

Comparing the projected NS heating sensitivity with limits from terrestrial direct detection experiments (shown as green and orange curves in Fig. 3.6) we find similar behaviour for D1 and D5. This is expected, as both of these operators give rise to unsuppressed spin-independent DM-nucleon scattering cross-sections. The  $p$ -wave suppression of the D1 annihilation cross-section increases  $t_{\text{eq}}$  compared to that for D5; nonetheless, equilibrium is reached relatively quickly compared to  $t_*$ . The D4 (pseudoscalar) interaction has dismal prospects of being observed in direct detection experiments, due to the severe  $q_{\text{tr}}^4$  suppression for the scattering of non-relativistic DM. In contrast, NS heating has much greater sensitivity.

Note that the time required for complete thermalisation (grey contours) is much longer for D4 (momentum-suppressed scattering) than for D1 and D5. In fact, for operator D4, full thermalisation is not achieved for most of the interesting parameter space. This illustrates the importance of correctly identifying  $t_{\text{eq}}$  as the timescale on which full heating is achieved, rather than the much longer  $t_{\text{therm}}$ .

### 3.6 Interaction rate in the zero temperature approximation

In this section, we calculate the interaction rate in the zero temperature approximation for  $|\bar{M}|^2 = \alpha t^n$ , where  $n = 0, 1, 2$  and  $\alpha$  is a constant, in the low energy, Pauli suppressed regime where  $K_\chi = E_\chi - m_\chi < \varepsilon_{F,i}$ . We assume the simplest scenario of constant target mass and point-like targets, as justified in Section 3.3.2.

In this approximation, the interaction rate in the energy regime relevant for thermalization is given by [226]

$$\Gamma^-(K_\chi, T_\star = 0) \propto \frac{1}{2^7 \pi^3 K_\chi k} \int_0^{K_\chi} q_0 dq_0 \int \frac{t_E^n dt_E}{\sqrt{q_0^2 + t_E}} \Theta(\varepsilon_{F,i} - q_0), \quad (3.41)$$

where  $t_E = -t$ , and

$$\int \frac{t_E^n dt_E}{\sqrt{q_0^2 + t_E}} = 2D_n(q_0^2, t_E) \sqrt{q_0^2 + t_E}. \quad (3.42)$$

The  $D_n$  functions can be found in Appendix B of ref. [226]. As we shall see, the integration intervals in Eq. 3.41 depend on whether or not Pauli blocking suppresses any part of the thermalization process. In both cases, we can find simple analytic approximations to these integrals. The minimal DM mass for which Pauli blocking is never in effect is denoted by  $m_\chi^{\text{crit}}$ .

We first consider the case where  $m_\chi \lesssim m_\chi^{\text{crit}}$ . For the cases of  $\mu \ll \varepsilon_{F,i}/K_\chi$  or  $\mu \gg K_\chi/\varepsilon_{F,i}$ ,  $\Gamma^-$  at first order in  $K_\chi$  is given by

$$\Gamma^-(K_\chi) \sim \frac{\alpha}{2^7 \sqrt{2} \pi^3 m_\chi^{3/2} K_\chi^{1/2}} \int_0^{K_\chi} q_0 dq_0 \left( \int_{t_E^-}^{t_E^+} \frac{t_E^n dt_E}{\sqrt{q_0^2 + t_E}} \right) \quad (3.43)$$

$$= \frac{\alpha}{2^6 \sqrt{2} \pi^3 m_\chi^{3/2} K_\chi^{1/2}} \int_0^{K_\chi} q_0 dq_0 \left( \sqrt{q_0^2 + t_E^+} D_n(q_0^2, t_E^+) - \sqrt{q_0^2 + t_E^-} D_n(q_0^2, t_E^-) \right), \quad (3.44)$$

where  $t_E^\pm$  are defined in ref. [226]. For matrix elements independent of  $t$  ( $n = 0$ ), we have  $D_0(q_0^2, t_E^\pm) = 1$  and this result simplifies to

$$\begin{aligned} \Gamma_{n=0}^-(K_\chi) &\sim \frac{|\bar{M}|^2}{2^6 \pi^3 m_\chi} \int_0^{K_\chi} dq_0 q_0 \left[ \sqrt{2 \left( 1 + \sqrt{1 - \frac{q_0}{K_\chi}} \right)} - \frac{q_0}{K_\chi} - \sqrt{2 \left( 1 - \sqrt{1 - \frac{q_0}{K_\chi}} \right)} - \frac{q_0}{K_\chi} \right] \\ &= \frac{|\bar{M}|^2}{120 \pi^3 m_\chi} K_\chi^2. \end{aligned} \quad (3.45)$$

We can rewrite the previous expression in terms of the DM-baryon scattering cross-section using the following expression

$$\sigma_{i\chi}^{n=0} = \frac{|\bar{\mathcal{M}}|^2}{16\pi m_i^2(1+\mu)^2}, \quad (3.46)$$

giving the interaction rate at first order in  $K_\chi$

$$\Gamma_{n=0}^-(K_\chi) \sim \frac{2m_i}{15} \frac{(1+\mu)^2}{\mu} K_\chi^2 \sigma_{i\chi}^{n=0}. \quad (3.47)$$

This result has the same  $K_\chi$  and  $\mu$  scaling as that of ref. [109].

Performing a similar analysis for  $|\bar{\mathcal{M}}|^2 = \alpha(-t)^n$ ,  $n = 1, 2$ , we find

$$\Gamma_{n=1}^-(K_\chi) \sim \frac{2\alpha}{105\pi^3} K_\chi^3, \quad \Gamma_{n=2}^-(K_\chi) \sim \frac{4\alpha}{63\pi^3} m_\chi K_\chi^4. \quad (3.48)$$

The expressions for the cross-sections for  $n = 1, 2$  are

$$\sigma_{i\chi}^{n=1} = \frac{\alpha}{16\pi m_i^2(1+\mu)^2} t_{max}, \quad \sigma_{i\chi}^{n=2} = \frac{4}{3} \frac{\alpha}{16\pi m_i^2(1+\mu)^2} t_{max}^2. \quad (3.49)$$

These cross-sections must be normalized to sensible momentum transfer. We take this reference point to be the surface of the star, such that

$$t_{max} \sim \frac{4m_\chi^2}{1+\mu^2} \frac{1-B(R_\star)}{B(R_\star)}. \quad (3.50)$$

The interaction rates for  $n = 1, 2$  can then be written as

$$\Gamma_{n=1}^-(K_\chi) \sim \frac{8}{105\pi^2} \frac{(1+\mu)^2(1+\mu^2)}{\mu^2} \sigma_{surf} K_\chi^3 \frac{B(R_\star)}{1-B(R_\star)}, \quad (3.51)$$

$$\Gamma_{n=2}^-(K_\chi) \sim \frac{1}{21\pi^2} \frac{(1+\mu)^2(1+\mu^2)^2}{\mu^3} \frac{\sigma_{surf}}{m_i} K_\chi^4 \left[ \frac{B(R_\star)}{1-B(R_\star)} \right]^2. \quad (3.52)$$

We now look at the interaction rate in the super-heavy DM mass regime,  $m_\chi \gtrsim m_\chi^{\text{crit}}$ . The exact value of  $m_\chi^{\text{crit}}$  will depend on the NS configuration. However, we can take some typical values relevant to thermalization to give an estimate of its value. Taking  $K_\chi = 10^3$  K,  $\varepsilon_{F,i} = 200$  MeV, we see that

$$m_\chi \geq \frac{2\varepsilon_{F,i}(2m_i + \varepsilon_{F,i})}{K_\chi} \sim \frac{4\varepsilon_{F,i}m_i}{K_\chi} = m_\chi^{\text{crit}} \sim 9.65 \times 10^9 \text{ GeV}. \quad (3.53)$$

The maximum energy transfer in this regime will always be  $q_0^{\text{MAX}} < K_\chi$ , with

$$q_0^{\text{MAX}} \sim K_\chi \left[ 2\sqrt{\frac{m_\chi^{\text{crit}}}{m_\chi}} - \frac{m_\chi^{\text{crit}}}{m_\chi} + \mathcal{O}\left(\left(\frac{m_\chi^{\text{crit}}}{m_\chi}\right)^{\frac{3}{2}}\right) \right]. \quad (3.54)$$

Performing a similar analysis as the  $m_\chi \lesssim m_\chi^{\text{crit}}$  regime leads to the following expression for  $\Gamma^-$ ,

$$\Gamma^-(K_\chi) \sim \frac{|\bar{M}|^2}{2^7 \sqrt{2} \pi^3 m_\chi^{3/2} K_\chi^{1/2}} \int_0^{q_0^{\text{MAX}}} q_0 dq_0 \left( \int_{t_E^-}^{t_{\mu^-}^+} \frac{t_E^n dt_E}{\sqrt{q_0^2 + t_E}} \right), \quad (3.55)$$

where  $t_{\mu^-}^+$  is defined in ref. [226]. For the simplest case of constant  $|\bar{M}|^2$  this results in

$$\begin{aligned} \Gamma_{n=0}^-(K_\chi) &\sim \frac{K_\chi \varepsilon_{F,i} |\bar{M}|^2}{24 \pi^3 \mu^2 m_i} \left[ \sqrt{\frac{m_\chi^{\text{crit}}}{m_\chi}} + \mathcal{O}\left(\frac{m_\chi^{\text{crit}}}{m_\chi}\right) \right] \\ &= \frac{|\bar{M}|^2 (m_i \varepsilon_{F,i})^{3/2}}{12 \pi^3 m_\chi^{5/2}} K_\chi^{1/2}. \end{aligned} \quad (3.56)$$

### 3.7 Thermalization of super-heavy DM

For DM that is heavier than the critical mass  $m_\chi \gtrsim m_\chi^{\text{crit}}$ , the energy lost in each scatter is a tiny fraction of the total DM kinetic energy. Moreover, the average time between collisions is typically on the order of fractions of a second. This warrants the use of a continuous approximation in this regime rather than performing the discrete summation. The thermalization time is then found by integrating the rate at which the DM kinetic energy changes,

$$\frac{dK_\chi}{dt} = -\Gamma^-(K_\chi) \langle \Delta K_\chi \rangle, \quad (3.57)$$

from the initial kinetic energy,  $K_\chi = m_\chi \left( \frac{1}{\sqrt{B(r)}} - 1 \right)$ , to the final value  $T_{\text{eq}} \ll m_\chi$ . For a constant cross-section ( $n = 0$ ), we substitute Eqs. 3.56 and 3.14 into the expression above leading to

$$t_{\text{therm}}^{(n=0)} \sim \frac{9\pi^2 m_\chi}{8(m_i^{\text{eff}})^2 \varepsilon_{F,i}^2 \sigma_{i\chi}^{n=0}} \log \left[ \frac{m_\chi}{T_{\text{eq}}} \left( \frac{1}{\sqrt{B(R_\star)}} - 1 \right) \right]. \quad (3.58)$$

Taking the final temperature to be  $T_{\text{eq}} = 10^3$  K and  $B(R_\star) = 0.5$ , this yields

$$t_{\text{therm}}^{(n=0)} \sim 1.7 \text{ yrs} \left( \frac{m_\chi}{10^{10} \text{ GeV}} \right) \left( \frac{0.5 m_n}{m_i^{\text{eff}}(0)} \right)^2 \left( \frac{0.2 \text{ GeV}}{\varepsilon_{F,i}(0)} \right)^2 \left( \frac{10^{-45} \text{ cm}^2}{\sigma_{i\chi}^{n=0}} \right). \quad (3.59)$$

Repeating for  $d\sigma \propto t^n$  ( $n = 1, 2$ ), we calculate the thermalization time for  $n = 1$  to be

$$t_{\text{therm}}^{(n=1)} \sim \frac{9\pi^2 m_\chi}{64m_i^{\text{eff}} \varepsilon_{F,i}^3 \sigma_{i\chi}^{n=1}} \left[ \frac{1 - B(R_\star)}{B(R_\star)} \right] \log \left[ \frac{m_\chi}{T_{\text{eq}}} \left( \frac{1}{\sqrt{B(R_\star)}} - 1 \right) \right], \quad (3.60)$$

$$\sim 3.5 \text{ yrs} \left( \frac{m_\chi}{10^{10} \text{ GeV}} \right) \left( \frac{0.5 m_n}{m_i^{\text{eff}}(0)} \right) \left( \frac{0.2 \text{ GeV}}{\varepsilon_{F,i}(0)} \right)^3 \left( \frac{10^{-45} \text{ cm}^2}{\sigma_{i\chi}^{n=1}} \right), \quad (3.61)$$

and that for  $n = 2$  to be

$$t_{\text{therm}}^{(n=2)} \sim \frac{5\pi^2 m_\chi}{32\varepsilon_{F,i}^4 \sigma_{i\chi}^{n=2}} \left[ \frac{1 - B(R_\star)}{B(R_\star)} \right]^2 \log \left[ \frac{m_\chi}{T_{\text{eq}}} \left( \frac{1}{\sqrt{B(R_\star)}} - 1 \right) \right], \quad (3.62)$$

$$\sim 3.5 \text{ yrs} \left( \frac{m_\chi}{10^{10} \text{ GeV}} \right) \left( \frac{0.2 \text{ GeV}}{\varepsilon_{F,i}(0)} \right)^4 \left( \frac{10^{-45} \text{ cm}^2}{\sigma_{i\chi}^{n=2}} \right). \quad (3.63)$$

### 3.8 Thermalization time for $s$ - and $t$ -dependent interactions

In Section 3.3.2, we assumed  $|\overline{\mathcal{M}}|^2 \propto t^n$  when deriving analytical approximations for the thermalization timescale. To understand the behavior of the thermalization time for the operators in Table 1.1, we can make use of the results for  $t^n$  dependent interactions. For cross-sections that are linear combinations of different powers of  $t$ , we can approximate the thermalization time using the previous results in the following way

$$|\overline{\mathcal{M}}|^2 = a_0 + a_1 t + a_2 t^2, \quad (3.64)$$

$$\sigma = a_0 \sigma_0 + a_1 \sigma_1 + a_2 \sigma_2, \quad (3.65)$$

$$\frac{1}{t_{\text{therm}}} \sim \frac{a_0}{t_{\text{therm}}^{(n=0)}(\sigma_{i\chi} = \sigma_0)} + \frac{a_1}{t_{\text{therm}}^{(n=1)}(\sigma_{i\chi} = \sigma_1)} + \frac{a_2}{t_{\text{therm}}^{(n=2)}(\sigma_{i\chi} = \sigma_2)}. \quad (3.66)$$

Hence, the inverse of the thermalization time will be given by a weighted linear combination of the inverse times for each contribution. As higher powers of  $t$  require significantly longer thermalization times, for coefficients of similar size, the resulting sum will be dominated by the lowest power of  $t$  appearing in  $|\overline{\mathcal{M}}|^2$ . We can thus identify the dominant terms for operators D1-D4 based on power counting, which we have listed in Table 1.1.

For  $s$ -dependent amplitudes, we can in principle use the interaction rates calculated in Appendix A of ref. [229], perform a series expansion in  $K_\chi$  and repeat the same procedure outlined in Section 3.3.2 for  $s$ -independent matrix elements.

Interestingly, we find that for the purpose of calculating the thermalization time, there is an easier way to obtain the correct result. One can indeed check that, at zero order in  $\varepsilon_{F,i}/m_i^{\text{eff}}$ , the resulting time for  $s^1, s^2$  is equivalent to the constant case, with the matrix element calculated by setting

$$s \rightarrow (m_\chi + m_i^{\text{eff}})^2, \quad (3.67)$$

while the  $st$  case has a result equivalent to the  $t$  case, with the matrix element calculated using the same substitution. This is, in practice, equivalent to setting both the DM and neutron targets at rest. There is, however, an important exception, when it comes to calculating the thermalization time of a linear combination of these terms. In particular, when the amplitudes at order  $\mathcal{O}(t^0)$ , are proportional to combinations of  $1, s, s^2$  such as

$$\begin{aligned} & s - (m_\chi + m_i^{\text{eff}})^2, \\ & [s - (m_\chi + m_i^{\text{eff}})^2]^2, \\ & [s - (m_i^{\text{eff}})^2 - m_\chi^2]^2 - 4(m_i^{\text{eff}})^2 m_\chi^2. \end{aligned} \quad (3.68)$$

All these combinations give a null result after applying substitution 3.67. In such a case, one may think that the dominant term is given by some remaining  $t^n$  term. It is worth noting that the expressions in Eq. 3.68 appear in operators that, at low energy, are known as velocity-dependent, because their matrix elements are proportional to positive even powers of the DM-target relative speed. Consequently, it is important not to neglect the motion of the targets in the neutron star, moving at relativistic speeds that are of the order of the Fermi velocity  $v_F^2 = 2\varepsilon_{F,i}/m_i^{\text{eff}}$ . In those cases, one should instead set  $s$  to<sup>6</sup>

$$s \rightarrow (m_\chi + m_i^{\text{eff}})^2 + 2m_\chi\varepsilon_{F,i}. \quad (3.69)$$

In summary, operators D5, D8 and D9 can be safely expanded using 3.67, while operators D6, D7 and D10 have velocity-dependent amplitudes and require Eq. 3.69. The dominant terms for each operator can be found in Table **Add the dominant terms in a new table**. For equal values of the leading term in  $|\bar{\mathcal{M}}|^2$ , the thermalization time for each operator will be the same as the relevant  $t^n$  power law.

---

<sup>6</sup>We assume that  $\mu \gg m_i^{\text{eff}}/m_\chi^{\text{crit}}$  when making this substitution.

### 3.9 Temperature distribution of captured dark matter

As seen in Fig. 3.3, interactions that depend on the momentum transfer, namely  $d\sigma \propto t^n$  with  $n = 1, 2$ , there are regions of the DM mass parameter space where thermalization does not occur within the age of the star. For the DM masses and NS temperatures of interest, this region of non-thermalization always occurs in the  $m_\chi \ll m_\chi^{\text{crit}}$  regime. From Eqs. 3.19, 3.21 and 3.22, we can estimate the time required for the DM to reach a kinetic energy  $K_\chi$

$$t_{K_\chi} \propto \frac{1}{K_\chi^{n+2}}. \quad (3.70)$$

If the DM does not thermalize within the age of the star, it will instead reach a minimum temperature,  $K_\chi^{\min}$ . Comparing the time required to achieve this temperature to the thermalization time,  $t_{\text{therm}}$  i.e. to have reached the equilibrium temperature  $T_{\text{eq}}$ , we find

$$\frac{t_{K_\chi^{\min}}}{t_{\text{therm}}} \sim \left( \frac{T_{\text{eq}}}{K_\chi^{\min}} \right)^{n+2}. \quad (3.71)$$

Accounting for the case where the DM reaches thermalization, we can write  $K_\chi^{\min}$

$$K_\chi^{\min} \sim T_{\text{eq}} \left( \max \left[ 1, \frac{t_{\text{therm}}}{t_{K_\chi^{\min}}} \right] \right)^{\frac{1}{n+2}} \quad (3.72)$$

$$\approx T_{\text{eq}} \left( 1 + \frac{t_{\text{therm}}}{t_{K_\chi^{\min}}} \right)^{\frac{1}{n+2}}. \quad (3.73)$$

The population of captured DM will have a distribution of energies at any given time, with this distribution being peaked at this minimum energy. As the orbital periods of the DM will be much shorter than the average time between interactions, the DM will be able to virialize between each interaction. Therefore, we can treat the DM as being contained within an isothermal sphere with temperature  $K_\chi^{\min} > T_{\text{eq}}$ .

Finally, it is worth noting that at times  $t > t_{\text{therm}}$ , even though the thermalization condition has been reached, the captured DM would consist of two components: a fraction of it (whose amount depends on time) would be in thermal equilibrium with the NS at temperature  $T_{\text{eq}}$ ; and another component still in the cooling down process. Assuming a capture rate constant over time, the fraction of thermalized DM is

$$f_{\text{therm}}(t) = \frac{t - t_{\text{therm}}}{t}. \quad (3.74)$$

## 3.10 Quark-level vs hadron-level annihilation cross-sections

The annihilation cross-sections shown in Table 3.1 are for DM annihilation to quark final states. More properly, we should consider the hadron-level annihilation cross-section. However, we are primarily concerned with the capture-annihilation equilibrium timescale, and not the details of the annihilation process. Therefore, if the annihilation rate to hadrons is not significantly different from the quark level result, this subtlety can be avoided.

To check the validity of the quark-level approximation, we estimate the annihilation rate to hadrons, working at lowest order in Chiral Perturbation Theory. We use couplings to the meson octet obtained from ref. [231]; for annihilation to baryons, the operators listed in Table 1.1 are used. For DM masses in the range  $m_\pi < m_\chi \lesssim m_{\text{charm}} = 1.27 \text{ GeV}$ , we find that the cross-section for annihilation to hadrons differs by less than an order of magnitude than that for annihilation to quarks. For larger DM mass, the difference is negligible. Therefore, to simplify the discussion, we consider DM annihilation to quark final states for DM masses above the pion mass.

Below the pion mass, the only kinematically allowed DM annihilation channels would be to leptons or photons. The size of the DM couplings to these states would, in general, be unrelated to the DM-quark couplings we have assumed. (They are expected to be non-zero, because they would be induced at loop level [126], even if absent at tree level.) However, due to the considerable Fermi energies of the electrons and muons near the centre of the NS, these channels will be Pauli blocked for the whole DM mass range below  $m_\pi$ , forbidding these annihilations from occurring. To remain as model-independent as possible, we will not consider lepton and photon annihilation channels.

Figure 3.7 shows  $t_{\text{eq}}$  contour lines in the  $\Lambda_q - m_\chi$  plane for the NS benchmark model QMC-2,  $T_{\text{eq}} = 1000 \text{ K}$  and two representative operators D7 (left) and D8 (right). Operators whose thermally averaged annihilation cross-section  $\langle \sigma_{\text{ann}} v_\chi \rangle$  has a  $m_f/m_\chi$  leading order term, namely D1-D4 and D8 (see Table 3.1), exhibit a sudden change in the slope wherever a new annihilation channel opens (see dotted lines on the right panel of Fig. 3.7). Note that the higher the cutoff scale  $\Lambda_q$ , the lower the scattering and annihilation cross-sections, resulting in a larger  $t_{\text{eq}}$  timescale. For lower  $T_{\text{eq}}$  temperatures, DM requires more time to reach both equilibrium conditions, thermalization and capture-annihilation. The variation of these results with respect to the NS configuration amounts at most to a factor of  $\sim 2$  in the  $t_{\text{eq}}$  contours (see shaded regions in the left panels) from the lightest configuration (QMC-1,  $1M_\odot$ ) to the heaviest (QMC-3,  $1.9M_\odot$ ) for most operators, with the sole exception of D4 for which this factor rises up to  $\sim 2.4$ .

### 3.11 Capture-annihilation equilibrium for the EFT operators

In Fig. 3.8, we show isocontours of maximal capture (yellow and light blue lines) and capture-annihilation equilibrium (magenta lines) timescale in the  $\Lambda_q - m_\chi$  plane for all EFT operators. Values of  $\Lambda_q$  below the  $t_{\text{eq}}$  lines result in smaller capture-annihilation equilibrium timescales. We can see in Fig. 3.6 that for all operators the  $t_{\text{eq}}$  timescale is always smaller than the time required for captured DM to thermalize. Captured DM achieves the steady state condition in a timescale as short as  $\sim 1 \text{ yr}$  (D1, D6-D10) or as long as  $10^5 \text{ yr}$  (D3). Note that the displayed lines for the  $t_{\text{eq}}$  are the values for which the entire parameter space relevant for capture reaches equilibrium with annihilation.

For D1 and D6-D10, we observe that captured DM achieves thermal equilibrium in less than  $\sim 1 \text{ Myr}$  (grey lines). On the other hand, as expected from Fig. 3.3 captured DM whose interactions are momentum suppressed, namely operators D2-D4, would never thermalize to the temperature expected from DM-induced heating in 1 Gyr, or even in less than the age of the Universe, with the sole exception of the corner region of very light DM  $m_\chi \lesssim 2 \text{ MeV}$  and an even narrower corner of the parameter space for D4.

Therefore, for all EFT operators, the energy released in the annihilation process adds up to the energy deposited via capture increasing the DM-induced heating for  $m_\chi \gtrsim m_\pi$  (yellow shaded area). Recall that we have made no assumptions about the energy scale that controls DM interactions with leptons. For DM of mass below  $m_\pi$  (light blue lines), at least kinetic heating is expected to contribute to the star luminosity.

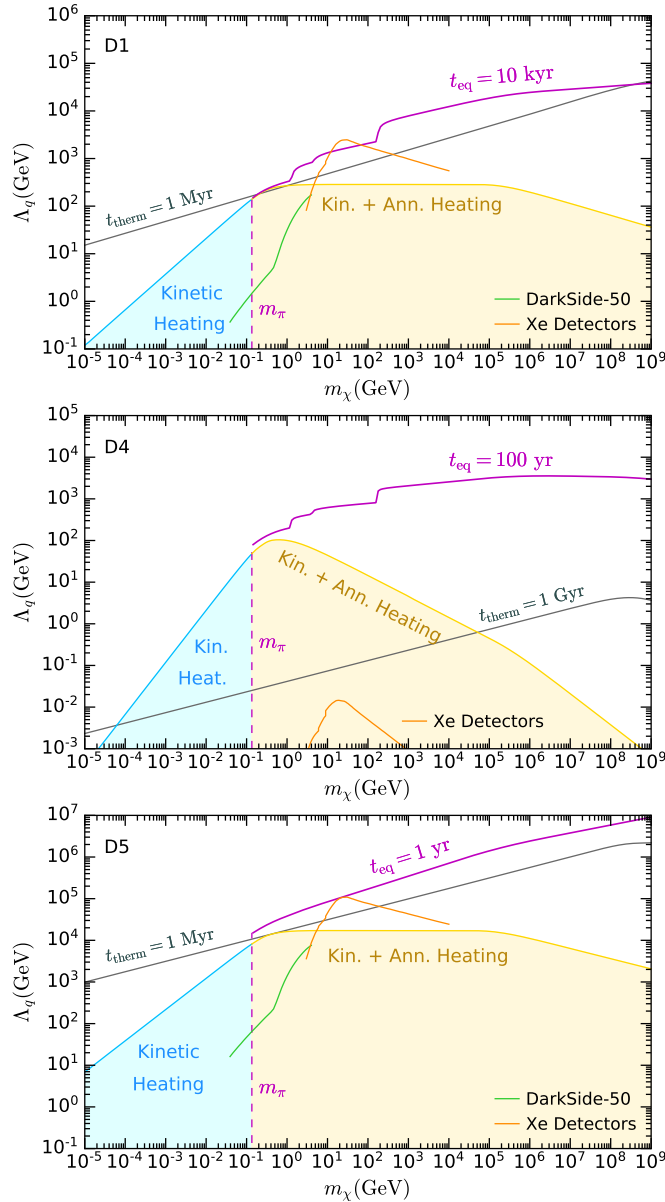


**Figure 3.6:** Projected NS heating sensitivity for maximal capture efficiency, for DM-baryon interactions described by operators D1, D4 and D5. We have used the QMC-2 ( $1.5M_{\odot}$ ) benchmark NS configuration. We show the regions where DM kinetic and annihilation heating both contribute to the NS luminosity (yellow) and where kinetic heating alone contributes (light blue). Contour lines for capture-annihilation equilibrium (magenta) and thermalisation (grey) are shown for indicative timescales. Lower limits on  $\Lambda_q$  from leading direct detection experiments [34–37] are also shown.

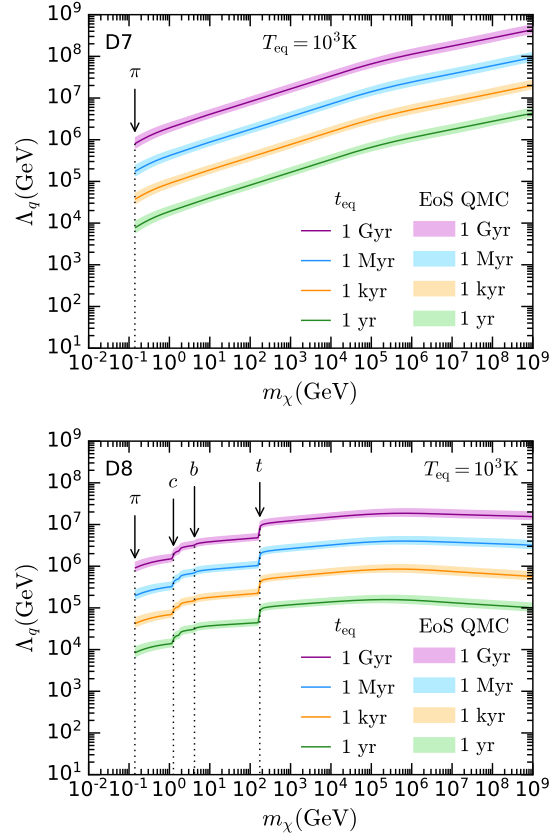


**Figure 3.7:** Contours of the capture annihilation timescale,  $t_{\text{eq}}$ , in the  $\Lambda_q - m_\chi$  plane for operators D7 (left) and D8 (right) and  $T_{\text{eq}} = 1000 \text{ K}$ . Solid lines represent the calculation for the NS benchmark model QMC-2, and shaded regions denote the variation with the NS choice for the QMC EoS family. Dotted lines in the right panel indicate the mass thresholds for various annihilation channels.

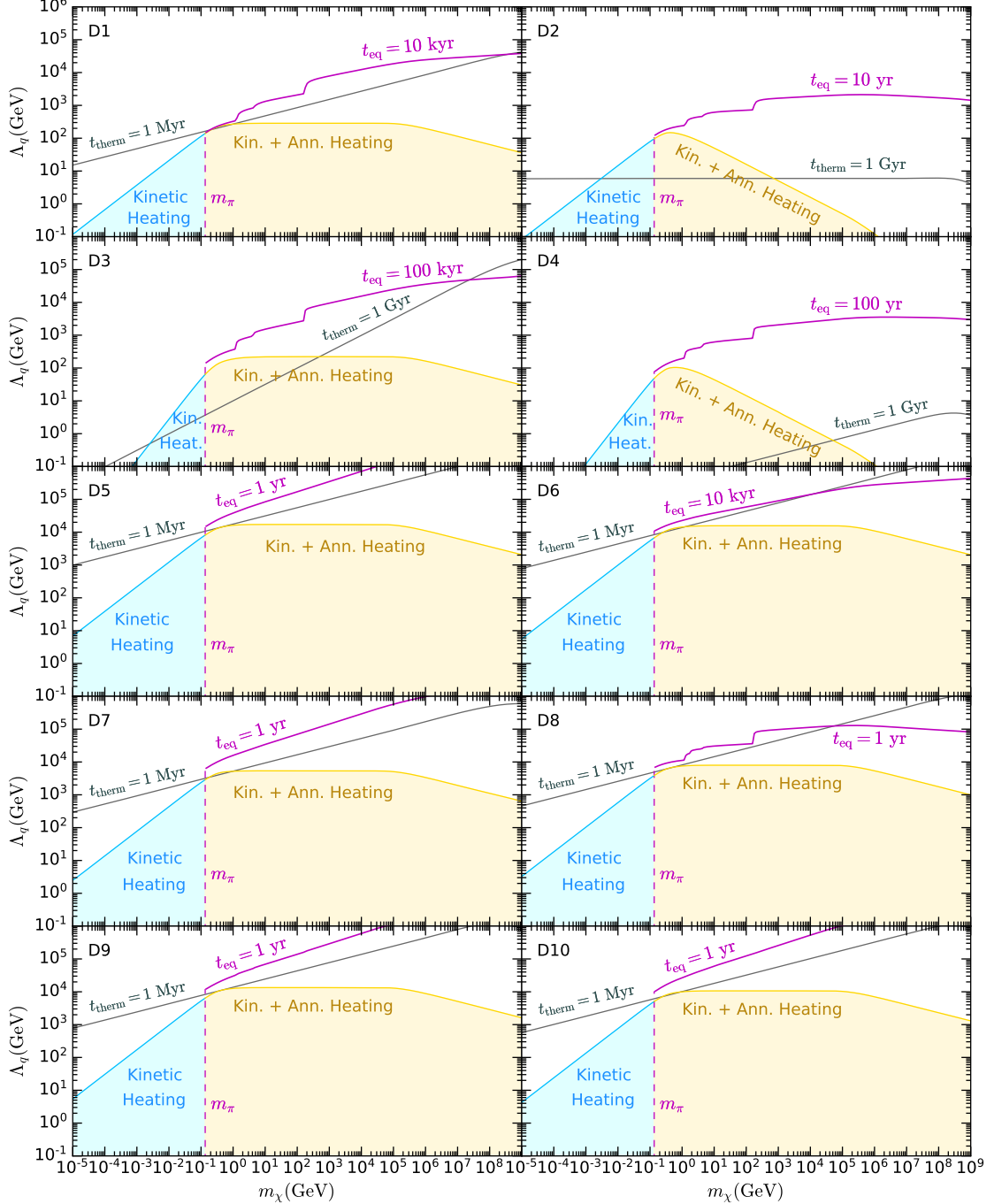


**Figure 3.8:** Projected NS heating sensitivity for maximal capture efficiency, for the full set of DM-baryon interactions described by the EFT operators of Table 1.1. We have used the QMC-2 ( $1.5M_\odot$ ) benchmark NS configuration. Color coding as in Fig. 3.6.